SENSITIZATION OF MALIGNANT BREAST EPITHELIAL CELLS TO PROTON RADIATION BY METALLIC NANO-PARTICLES

By: Nichole Libby

July 2023

Director of Dissertation: Dr. Jefferson Shinpaugh

Major Department: Physics

Abstract

Enhancing cancer treatment has garnered interest for more than 50 years. Enhancement has been considered in the evolution of treatment modalities as well as in the potential additives at the cellular level as radio-sensitizers. These enhancements all encompass the same goal: a method to spare healthy surrounding tissue while killing the cancerous tissue. In this work Polyethylene glycol (PEG)-coated gold nano-particles (GNPs) and super paramagnetic iron oxide nano-particles (SPIONs) were investigated as radio-sensitizers for malignant breast (MCF7) cells irradiated by energetic protons.

The cells were cultured in the Department of Biology's Cell Culture Laboratory, where they were plated onto either custom 15-well plates or standard 96-well plates 48 hours prior to irradiation. The cells were then irradiated by 3 MeV protons in the East Carolina University Accelerator Laboratory in the Department of Physics. Twenty-four hours prior to irradiation the cells were treated with varying concentrations of the metallic nano-particles (NPs). Cell viability was determined using a color-metric assay (PrestoBlue), which was conducted prior to, as well as 24 hours post irradiation. Survival curves were determined based on the metabolic rate for each NP type and concentration post irradiation to observe potential sensitization effects. Sensitization effects were only observed for the PEG-coated GNPs at concentrations of 15 nM, 45 nM, and 68 nM. While each showed promise as radio sensitizers at the higher dose ranges (>6 Gy), the 45 nM concentration showed the greatest sensitization effects throughout the entire dose range (2-11 Gy).

SENSITIZATION OF MALIGNANT BREAST EPITHELIAL CELLS TO PROTON RADIATION BY METALLIC NANO-PARTICLES

A Dissertation Proposal Presented to
the Faculty of the Department of Physics
East Carolina University

In Partial Fullfillment
of the Requirements for the Degree
Doctor of Philosophy
Biomedical Physics

By
Nichole Libby
July 2023

Director of Dissertation: Jefferson Shinpaugh, PhD
Dissertation Committee Members:
Robert Corns, PhD
Regina DeWitt, PhD
Michael Dingfelder, PhD
Jean-Luc Scemama, PhD

ACKNOWLEDGEMENTS

I want to acknowledge the wonderful group of people that helped me throughout my time at ECU on this project. The first person I want to acknowledge is Tristan Gaddis, she was my right hand man and partner in crime. Together we took this project further than I ever thought we would be able to. She worked tirelessly with me on refining protocols and getting the experimental set up together and getting all our data!

Next, Chris Bonnerup, Gene Oakley, and William Holland. These three men were always there to help make sure we had the set-ups we needed to run our experiments. They made sure we had the pieces to build the line as well as the electronics set up to make sure everything functioned properly. I've learned so much from these three men.

One understated person is Brian Hinckley, my wonderful husband. He helped with my cell culture and tirelessly helped edit my dissertation. He give me all the moral support to keep chugging along. He also introduced me to Dr. Anderson, who was able to pin point our contamination issue right away. Giving us the tools needed to get back on track with our project.

Most importantly I want to acknowledge my committee, Dr. Corns, Dr. DeWitt, Dr. Dingfelder, and Dr. Scemama, for the help and support not only through this project, but also through my PhD. I have had the privilege to be taught in some fashion by each one of you and I only hope I can pass along the knowledge you have given to me. Most importantly I want to thank my advisor Dr. Shinpaugh, working in your lab has taught me many invaluable skills. I know I will be able to take everything I've learned and apply them to my future endeavors. Thank you all for the support through one of the toughest and most rewarding journeys of my life.

Table of Contents

List of Tables

List of Figures

List of Abbreviations

*OH hydroxyl radical 6

PEG Polyethylene glycol i

RBE relative biological effectiveness 11

ROS reactive oxygen species 11

RT radiation therapy 10

SER sensitization enhancement ratio 39

SF_6 Sulfur Hexafloride 80

SPIONs super paramagnetic iron oxide nano-particles i

SRIM The Stopping and Range of Ions in matter 35

SSB single strand break 6

TiH titanium hydride 31

TRIM Transport of ions in Matter 35

YAG yttrium aluminum garnet 33

Z atomic number 4

1 Introduction

Radiation is considered energy that is in transit [1]. Ionizing radiation is one of the most common forms of radiation utilized in medical physics; it is classified as radiation that passes through a material with a high enough energy to overcome the binding energy of the atomic nuclei or orbital electrons. Consequently it ejects an orbital electron from the atom within the material [2]. When the radiation interacts with the nuclei or orbital electrons, elastic, inelastic or absorption events can occur.

When considering ionizing radiation, one can consider two classes: electromagnetic radiation and particulate radiation. The distinction between the two allows one to understand the source of the ionizing radiation, and consequently what kind of interactions may take place along its path through the material [3].These events can impart energy to the orbital electrons which create interaction that will deposit energy locally or further along the particle's path.

1.1 Electromagnetic Radiation

When considering types of electromagnetic radiation, we are predominately considering γ-rays and x-rays passing through a material. γ-rays and x-rays are distinguished based on the origin of the radiation; γ-rays are the product of nuclear decay, while x-rays are generated via atomic interactions that accelerate electrons to high energies, bombarding them into a target, such as gold or tungsten. The kinetic energy that is derived from this motion is what produces the x-rays [3], and results in indirectly ionizing events. A photon is a particle that has no mass or electrical charge that can travel at the speed of light (c). Photons are electromagnetic radiation that are considered to be discrete energy packets when interacting with the surrounding atoms within the materials [1]. The energies for photons are related to equation 1; where E is the photon energy and typically measured in kiloelectron volt (keV) or mega-electron volt (MeV), and λ is the wavelength of the electromagnetic field created

and is measured in nanometer (nm) [1].

$$E = \frac{hc}{\lambda} \tag{1}$$

x-ray and γ-ray photons typically have an energy range of keV-MeV, implying they have high energies with a short wavelength that when reacting with a medium will result in secondary ionization events. These events are the product of the high energy photons making contact with orbital electrons or atomic nuclei releasing an electron or causing the creation of a electron-positron pair [1]. The three main interactions that can occur are the Compton effect, the Photoelectric effect, and Pair production [4, 3].

The first type of interaction that can occur as a byproduct of electromagnetic radiation is the Compton effect (Compton scattering). This interaction occurs when a photon of energy hν, where h is Plancks constant and ν is the particle frequency, collides with a stationary or unbound electron. Upon colliding with the electron, it is sent off at some angle θ with some kinetic energy, while the incident photon is scattered at angle ϕ with some energy hν' (pictured in Figure 1.1 panel B). The kinetic energy of the electron is the difference of the incident energy (hν) minus the new photon energy (hν'), displaying conservation of energy with this collision. When the electron is set in motion, it is now a fast moving electron and can potentially collide with other atoms surrounding it, creating ionizing events and consequently breaking chemical bonds and producing damage within a biological structure [3, 1, 4].

The photoelectric effect (pictured in Figure 1.1, panel A) is an event that can occur when an incident photon, of energy hν, collides with an atom within the material and its energy is totally absorbed. When the energy is absorbed into the atom, it releases one of its orbital electrons typically from the innermost shell of the atom, creating a photoelectron. This leaves an outer shell electron to drop down to fill the vacancy potentially creating a characteristic x-ray or an Auger electron [4, 1] adding a small interaction within the biological tissue. The energy that is released in biologic material is low, roughly 0.5 keV, which means the

energy released is absorbed locally, while higher Z materials will produce much higher energy, resulting in energy being deposited at a greater distance [2]. The energy that is given to the photoelectron is the difference between the initial photon energy and the binding energy of the inner shell electron, implying that the photon energy must exceed the binding energy for this event to occur [4]. Once the electron has been ejected, the resulting kinetic energy that is imparted to it will be deposited near the occurrence of the event. The range the electron will travel is dependent upon the medium and energy that is imparted to the electron. This will potentially have a biological effect on the tissue where the event occurs.

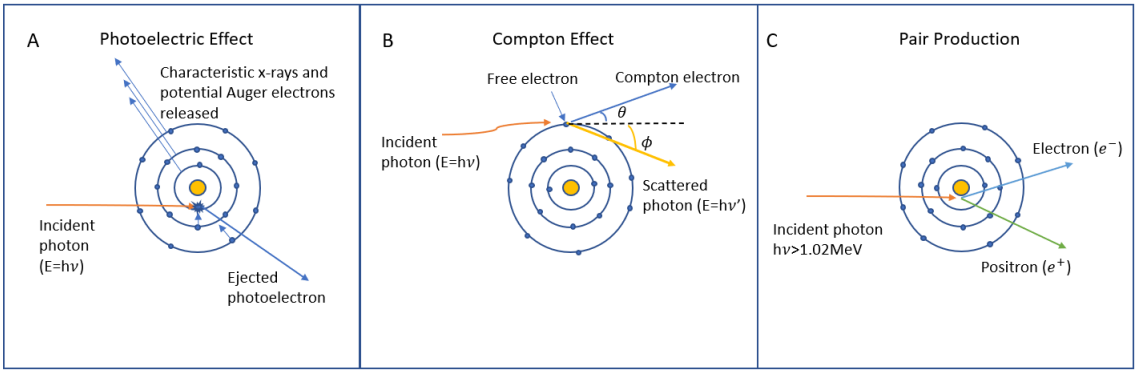

Figure 1.1: Panel A shows the photoelectric effect, panel B shows the Compton effect and panel C shows pair production. All three effects start with an incident photon either interacting with an orbital electron (A & B) or interacting with the nucleus (C) of the atom.

The final interaction of interest is pair production (pictured in figure 1.1, panel C). Pair production is an absorption process where a photon, with an energy greater than 1.02 MeV, interacts with the electromagnetic field of an atomic nucleus or orbital electron and all of the photons' energy is absorbed. As a result of the photon energy being absorbed, a positron (e^+) and an electron (e^-) are released from the atom. The rest mass of an electron is 0.511 MeV, since two particles are produced the photon energy must exceed 1.02 MeV, leaving the kinetic energy that is imparted to the positron and electron being $h\nu - 1.02MeV$ [2]. As a result of the released positron, annihilation radiation is created. As the positron travels through the material, it loses its energy slowing its movement process. As the slowing positron loses its energy it combines with a free electron in the material generating two annihilation photons,

sending them with an energy of 0.51 MeV in opposite directions. The probability of a pair production occurring will increase with increasing atomic number (Z) [2].

1.2 Particle Radiation

Particulate radiation deals with atomic or subatomic particles that typically have a large mass; a mass is considered "large" if the particle's rest mass exceeds that of an electron [2]. The particles that we consider to be particulate radiation are protons, neutrons, α particles and heavy charged particles [3]. With charged particles, the rate at which the particles lose energy will be the ultimate determinant for the distance the particle will travel as well as the amount of ionizing radiation that will be produced along that path [1]. All of these particles will cause direct ionizing radiation, through Coulomb force interaction between the electric field given off by the traveling particles and the electric field produced by the orbital electron or the nuclei of the atoms within the material [2]. For heavy charged particles, the ionization events will increase as the particles slow to a stop. The dose deposited to the medium will increase proportionally to the ionization events creating a Bragg ionization peak [1, 5]. This increase in dose over a short length is characteristic to particulate radiation and key in getting more localized dose to specific tumors.

Protons: Protons are positive in nature and have a mass that is about 2,000 times that of an electron [3]. Their large mass makes their acceleration require heavier equipment such as a cyclotron which accelerates the protons to high energies. As protons transverse a medium, interactions with orbital electrons or the atomic nuclei may happen through Coulomb force interactions. These interactions can be in the form of inelastic collisions or elastic collisions. With inelastic collisions, the proton typically interacts with an electron from the material; the proton will lose part of its energy potentially producing ionization and/or excitation within the atom. Elastic collisions are of minimal consequence as there is no energy loss by the proton, and no resulting ionization effects [2].

Neutrons: Neutrons are neutrally charged and of similar mass to protons, and because

of their neutral charge they cannot be accelerated by an electrical device. Instead, they can be the by-product of a charged particle accelerated to high energies, or when heavy radioactive atoms undergo fission. [3].

α-Particles: α-particles are made of the nuclei of the helium atoms; consisting of two protons and two neutrons giving them a positive net charge. They are typically released during the decay of naturally occurring radionuclides. For example, when Radium-226 decays to Radon-222, an alpha particle is released [3], which can be a common source of natural background radiation, to the general public.

Heavy Charged particles: Heavy charged particles are particles that have a rest mass large in comparison to the mass of an electron [2]. Because of their large mass, heavy charged particles tend to continually slow down as they move through a material, losing small amounts of energy with numerous numbers of individual collisions. They tend to move in a straight line, having very small deflection angles during collision as opposed to light particles like electrons which tend to undergo large deflection angels during collisions [1]. Their mass also contributes to the particles traveling at about 10% that of the speed of light. With this slower speed the particle tends to interact with the material it is moving through more frequently. This leads to greater energy losses and potentially an increase of ionization events [1]. The increase of ionization events shows a drastic increase of ionization at the end of the particles' track, which can be shown as a Bragg peak, similar to what happens to a proton or an α particle at the end of its path length.

1.3 Biological Effects of Radiation

Radiobiology is the study of the biological effects that ionizing radiation can have on living organisms and matter. Ionizing radiation occurs when the radiation has a large amount of kinetic or quantum energy, consequently forcing an orbital electron out of the molecule or atom; this takes about 10 eV [4]. Electromagnetic or particulate ionizing radiation can cause biological changes within the DNA structure, directly and indirectly, depending on

the amount of radiation or energy deposited within in the biologic material. These changes can be split into direct ionizing and indirect ionizing events. The incident radiation directly ionizes the molecules such as DNA of the materials, through Coulomb force interaction as the particle moves along its path through the material in question. Indirect ionizing events occur in two steps with the neutral, fast moving particle interacting with the biological system/material it is traveling through, thus giving up their energy by absorption into the material. This reaction will produce fast moving charged particles that will in turn be able to produce damage to its surroundings [3]. Cells are composed of roughly 80% water, which radiation may interact with and become ionized. When radiation interacts with water, free radicals can be produced via indirect action. A free radical is a molecule that carries an orbital electron that is unpaired which can dictate the chemical stability of the molecule. When radiation reacts with water it can cause an ion radical (H_2O^+), which is a charged ion that has an unpaired orbital electron (free radical). This ion radical can react with other water species within the cell and can cause a hydroxyl radical (*OH), which is highly reactive.

$$H_2O^+ + H_2O \rightarrow H_3O^+ +^* OH \tag{2}$$

The highly reactive hydroxyl radical can move a short distance within the cell, potentially causing critical damage within the DNA structure. DNA is considered the principal target for biological effects to occur after radiation exposure [3]. The double helix structure of the base pairs of either adenine and guanine or thymine and cytosine can be impacted tremendously by radiation through the release of a free radical and direct ionization events [3]. The amount of damage caused to DNA will depend heavily on how much radiation the DNA structure is exposed to and what kind of break the radiation has caused [3]. When radiation damage is seen in the DNA, it is classified as a single strand break (SSB) or a double strand break (DSB) [3]. A SSB occurs more frequently at lower amounts of radiation. Typically SSBs can be repaired easily by the cell because the occurrence will only break one side of the double helix structure. When the cell replicates the DNA strands it can use the remaining intact

structure to figure out what was lost on the broken side. This creates a blue print for a fixed strand of DNA to be reproduced. When this happens there is little biological consequence done by the radiation. In some cases, however, with a SSB, a mutation can occur from the strand not being able to properly repair itself. When DSBs occur, the break happens in both strands of the double helix, typically directly opposite of one another or spaced a couple base pairs apart. When this type of break occurs, it becomes difficult for the cell to repair the break, potentially causing cell death, carcinogenics, or mutation [3]. These breaks occur linearly with dose; the greater the amount of dose, the greater potential of DSBs to occur. With DSBs, the possibility of the biological end point resulting in cell death is greater than with the occurrences of SSBs. When cell death occurs, the cell has lost its reproductive integrity which can be measured and displayed via a survival curve for *in-vitro* cells. A survival curve (S) follows a linear-quadratic model, that has two portions of cell-killing by radiation (equation 3). The linear part that is depicted by αD, where α typically shows non-repairable damage. The quadratic term (βD^2), where β typically depicts repairable damage done by radiation [6, 7]. The linear portion of the model can be extrapolated from the top of the curve which can be related directly to irreparable damage in the cell. This will increase proportionally with an increase in dose [6]. From the linear-quadratic model, a ratio of α and β can be determined at a particular dose, when the two comments have equal contribution to cell death (equation 4). This is shown in equations 3 and 4, when the dose is proportional to the square of dose.

$$S = e^{-\alpha D - \beta D^2} \tag{3}$$

$$\alpha D = \beta D^2 \rightarrow D = \frac{\alpha}{\beta} \tag{4}$$

1.4 Dosimetry of charged particles

Radiation dose in a medium is defined as the energy absorbed per unit mass in the specific medium, which will ultimately play a large role in dosimetry [8]. Stopping power for a charged particle is defined as the rate at which the energy (E) of the charged particle is lost per unit length (x) in a medium, $(\frac{dE}{dx})$, typically in units of MeV/cm [4, 8]. The stopping power can be divided into collision stopping power and radiative stopping power. For the dosimetry of charged particles the interest is in collision stopping power, as those interactions produce ionization and excitation events along the particles path [4]. The mass collision stopping power, or the mass stopping power is signified as $-\frac{dE}{\rho dx}$ with units of MeV cm^2/g, ρ represents density of the target medium the particles travel through. While the mass stopping power expresses the average energy lost by the particle through all potential collisions in the medium, this may contribute to an over estimation of the dose. To compensate for the over estimation the restricted mass stopping power is defined as a fraction of the mass stopping power being accounted for with energies less than a particular cutoff energy Δ, and is represented as $(-\frac{dE}{dx})_\Delta$. The restricted mass stopping power is connected to the linear energy transfer (LET), equation 5.

$$LET_\Delta(\text{keV}/\mu\text{m}) = (\frac{dE}{\rho dx})_\Delta \tag{5}$$

The LET is defined as the rate at which energy is transferred to a material per unit mass. This is of particular relevance when considering radiobology. LET and mass stopping power go hand in hand where stopping power accounts for the particles' energy loss, and LET accounts for the energy transferred to the medium. [9, 8]

To consider absorbed dose from a parallel particle beam the rate of energy loss in the collisions must be considered. The parallel beam of monoenergetic protons will be incident

on a tissue material of thickness Δx over an area A.

$$\dot{E} = \dot{\phi} A (\frac{dE}{dx}) \Delta x \tag{6}$$

Where $\dot{\phi}$ is the fluence rate of the charged particles (particles/cm^2 s), $(\frac{dE}{dx})$ is the mass collision stopping power of the proton beam. Given the assumption the energy lost by the particles is deposited into the medium, the dose rate to the medium can be determined by dividing by the mass $\rho A \Delta x$ of the volume of the medium where ρ is the density of the tissue medium in question.

$$\dot{D} = \frac{\dot{\phi} A (\frac{dE}{dx}) \Delta x}{\rho A \Delta x} = \phi \frac{dE}{\rho dx} (\text{MeV/g}) \tag{7}$$

This can hold true for low energy protons as long as their energy loss is not sufficient enough to significantly change in the stopping power [4, 8].

2 Enhancements to Radiation Treatment

The overarching goal with radiation therapy (RT) is to maximize lethal radiation doses to tumors while minimizing dose to healthy tissues. An example of this goal in the clinical setting is cancer treatment, where the sparing of healthy tissue and organs around the tumorous regions is one of the main focuses. Emerging efforts to improve RT outcomes include optimization of current modalities as well as the addition of metallic NPs to further enhance healthy cell protection and tumor sensitization for both photon/electron beams as well as proton beams. Most often when receiving RT, the use of a linear accelerator (linac) is used. To mitigate dose to surrounding healthy tissue, as well as damage done along the path of radiation for the electrons and photons, Hadron therapy has been utilized to garner more localized dose deposition. Hadron therapy utilizes charged particles like protons or carbon ions rather than electrons or photons to administer radiation. The first to consider utilizing protons was Dr. Robert Wilson in 1946 [10]. For clinical application of proton therapy a synchrotron or cyclotron will be needed rather than a linac, which is the main modality for photons and electrons [2]. A major drawback to the synchrotron and cyclotron facilities is the hefty cost for building and maintenance. The advantage to Hadron therapy is the shift in how the dose is deposited along the particles path. The Bragg peak is the region where all of the protons energy is deposited, which is shown at the end of a depth-dose curve [2].

When utilizing protons, they produce a depth dose curve far different to that of photons and electrons. As the proton enters the body or tissue equivalent substance, the relative dose is small and only slightly rises relative to the distance traveled by the proton. Once the protons near the end of their path, there is a sharp increase of dose deposition and consequently the dose falls off quickly to zero, depositing most of it energy in a small area. The dose deposited is very localized and only spans a few centimeters [3, 2]. The desired minimal surface dose and surrounding tissue sparing that accompanies proton irradiation is the major reason proton beams are continually investigated. With proton therapy the

relative biological effectiveness (RBE) are similar to that of electrons, yielding a roughly 10 % increase to that of electrons/x-rays[2]. So, while the RBE and reactive oxygen species (ROS) are slightly increased compared to photon and electron treatments, the Braggpeak and consequent deposition of relative dose make proton therapy an interest in the betterment of RT. A compounding factor that may enhance proton therapy is the addition of metallic nanoparticles, which can enhance the radiation through particle interactions with the protons and the NPs [2, 3, 1, 11]. The possibility of radio-enhancement of proton beams with nanoparticles may yield lower surface doses, as well as more healthy cell survival around the affected tumorous region.

2.1 Radiosensitizers

The National Cancer Institute defines a radiosensitizer[1] as any substance that makes tumor cells easier to kill with RT. Radiation interacts with the biological materials outer shell electrons or the nucleus of the atom. When these interactions take place, free radicals and fast-moving electrons can be created, which potentially create DNA damage to the surrounding biologic material. Metallic NPs, more specifically high Z metallic NPs, will interact with the ionizing radiation, creating an increase in local dose delivered in the surrounding area of the NPs. When the metallic NPs can be localized to a specific region of interest, they can increase the number of photoelectric events, enhancing the initial radiation and effectively killing the tumor cells [12, 13]. The use of metallic NPs, specifically GNPs, for sensitization has been a hot topic for the better part of the last 30 years.

There have been many studies supporting the sensitizing effects of GNPs, compounded with x-ray or electron radiation [14, 15, 16, 17, 12], as well as some investigation, that utilize NPs and proton therapy [18, 19, 20, 11, 21].

From ion beam experiments it has been seen that short range Auger electrons can be released from the interaction with the metallic NP and create DNA damage to the surrounding

[1] use from www.cancer.gov

tissue.

2.2 Gold NPs

Gold has an atomic number, Z=79, which makes it a prime candidate to incorporate within a tumor region. When compounded with radiation, it has shown enhancement within the dose by way of increasing the photoelectric effect which will effectively kill more tumor cells [1, 22, 23, 24, 25, 26, 14, 12, 27, 13, 28]. The surface chemistry additions, such as amine or glucose capped functional groups, and size of the of the GNPs has shown to be an important factor on how well the NPs are incorporated into the tumors regions [25, 26, 29, 18, 12, 13, 30]. Many *in-vivo* and *in-vitro* studies have been implemented to find an optimal size and coating that will enhance cellular uptake of the GNPs. Some of the most predominant studies that pioneered the explorations into GNPs were executed by Hainfeld *et al.*; producing several papers outlining sensitization effects of GNPs on various types of tumors in mice. In 2004, the group used mice with EMT-6 mammary carcinomas, and they intravenously injected GNPs of an average diameter of 1.9 nm and irradiated with a single dose of 250 kVp x-rays. They utilized 4 groups of mice, 1 group that received no treatment of radiation nor GNPs, while another group received just GNPs and 2 groups that received two different concentrations of GNPs but equal amount of radiation. One group received 270 mg Au/cc for 2.7g Au/kg while the other group received 135 mg Au/cc for 1.35g Au/kg, both getting roughly 5 Gy/min. Overall, the control groups (no irradiation) saw no decrease in tumor size, in fact, there was an increase in size and consequently died within two weeks of the study starting. The two groups that received GNPs and x-ray irradiation saw a decrease in tumor size and a 50% and 86% increase in long term survival, respectively [22]. In 2008, Hainfeld *et al.* continued their previous study, further delving into enhancements of gold nanoparticles by effectively loading tumors with GNPs and irradiating with an x-ray source to find out what kind of enhancement to dose the GNPs could create [23]. It is evident that high Z materials like gold will be enhanced by x-rays, so this study attempts to understand

the dose enhancement factor (DEF) that GNPs can obtain in mice. The parameters were the same as from the 2004 study outlined above. However, this time, they investigated the percentage of GNPs within the tumor volume. They saw about 0.24 % of the tumor was saturated with GNPs, which when irradiated with 250kVp x-rays, again yielded high survival fractions over the course of a year for the groups that were both irradiated and injected with GNPs. Through the study it appeared the main way the GNPs were entering the tumor region was through the enhanced permeability and retention (ERP) effect. The authors concluded that surface coating can potentially provide better cell uptake which could yield higher dose enhancement and they recommended further study of these effects.

2.3 Parameters for Optimal NP Cellular Uptake

The study of NPs for drug delivery and radiation therapy enhancement has opened the door to understanding how surface coating can influence the pharmacokinetic properties of nanoparticles in biological systems [27, 31, 29, 28, 13, 30, 15, 32].

Coating dependence: When adding any kind of NPs into a biological system, whether it be for drug delivery or enhancement/protection of radiation therapy, it is important to understand how the nanoparticles will transition throughout the body. Research into this transition has shown that, when delivering nanoparticles to specific organs or tumor sites within the body, the size of the NPs and the surface modifications on the NPs are key ways to optimize the nanoparticles' path throughout the body, as well as their half-life within the body [31, 29, 30, 33, 32]. Surface modifications consist of coating the NPs in specific materials, such as polymers that will allow the NPs to target specific tissues or cell types. One commonly researched polymer is polyethylene glycol (PEG), which has been deemed to have low inherent toxicity and, when functionalized on the surface of NPs, will increase their circulation time within the blood, making uptake within cells and tumors greater than un-coated NPs [31, 34, 13, 35, 36]. One study done by Kommareddy *et al.* [34] showed that their PEG-coated NPs had longer blood circulation times, which resulted in higher uptake in

their target organs because of a lessened protein build up on the NPs from the PEG coating. This was monitored over a 48 hrs period where they compared un-coated Gel NPs to coated Gel NPs. Their focus was the deposition of NPs in the spleen, kidney, lungs and heart. This study showed that NPs coated with PEG were more likely to have longer circulation potentials, giving more time for organ uptake rather than just cycling through the body and immediately being excreted [34]. A comprehensive review has been done by Bromma et. al [30] that attests to, not only the importance of surface coating, but the size of the NPs and the means of injections when looking into *in-vivo* studies of these NPs [30].

PEG is not the only coating that can be applied to GNPs to improve radio-sensitization and cellular uptake, but glucose (Glu) capped GNPs and amine coating are also potentially a great surface coating that can improve cellular targeting and ultimately radio-sensitization [37, 38, 25, 27]. Roa *et al.* [37] showed improved sensitization with 2 Gy Cs 137 γ-rays. The Glu-GNPs and non-functionalized GNPs were introduced into human prostate carcinoma (MRC5 cells line) and irradiated, yielding an inhibition of cell proliferation after 24hrs of about 26.8%. Studies done by Kong *et al.* [25] also showed enhancement properties of Glu-GNPs in malignant breast cells (MCF7), finding the Glu-GNPs tended to gather in the cytoplasm of the cell, optimizing sensitization in desired locations within the cell. Further, the study further found that glucose caped GNPs gave the GNPs a surface potential that glucose metabolizing cells, like MCF7 cells are more likely to be up taken. Further investigation of amine-coated PEG-GNPs was done by Grellet *et al.* [27], where they found the amine coating to be an excellent addition for cellular uptake, which made it a candidate for their radio-sensitization study. The amine surface coating makes the inherent potential of the GNP positive and more likely to be taken in by a cell with a negative potential.

Size dependence: Several studies over the last 15 years have explored the importance of the size of the NP and the concentration. It was concluded in a paper by Chithrani *et al.* [15, 39] that concentration and size of NPs will be the ultimate determinate of radio-sensitization of cells treated with combinations of GNPs and radiation. In the experiment

run by Chithrani *et al.*, size dependence with citrate modified GNPs was prime at around 50nm for Hela cells. This size dependence was further studied by Zhang *et al.* with PEG coating.

Zhang *et al.* used PEG- coated NPs of varying sizes (5, 10, 30 and 60nm) to assess the bio-distribution of the NPs into various organs. Mice were injected intravenously in the tail with concentrations of 200 μg of GNP solution which yielded a dose of 4000μg/kg. There was one control group and 4 experimental groups with 5 mice in each group. The experiment supported the previous data that the larger NPs tend to uptake most heavily in the spleen and liver [29]. Table 1 was shows these outcomes. For the heart and liver, the smaller NPs of diameters between 5nm and 10 nm seemed to have the best cellular uptake. Based on the results yielded from Zhang *et al.* it appears that the smaller the diameter, the more likely for the NPs to be absorbed by various organs.

Organ	5nm	10nm	30nm	60nm
Heart	214 μg/kg	18 μg/kg	8.6 μg/kg	37 μg/kg
Liver	1797 μg/kg	2898 μg/kg	21 μg/kg	432 μg/kg
Kidney	390 μg/kg	48 μg/kg	151 μg/kg	14 μg/kg
Spleen	628 μg/kg	138 μg/kg	3363 μg/kg	721 μg/kg

Table 1: The first column is a list of the organs that were investigated, each column starts with the diameter of the NPs that were investigated and listed below each diameter is the concentration of NPs found in the respective organ.

2.4 GNPs irradiated with Protons

There have been observations that utilizing metallic nanoparticles paired with photons or x-rays has yielded increased rates of radiosensitization for various cell lines [12, 33, 15, 37, 40]. Now the efforts have shifted to understand the enhancement of dose delivery by metallic NPs embedded in various cells lines paired with protons. Monte Carlo (MC) SRIM simulations were explored by Torrisi *et al.* [41], where they saw a potential increase in proton LET in the Bragg peak region due to high concentrations of GNPs. The increase was seen in liquids

to be about 5% and a possible increase of 6.5% in soft tissue. Further studies with Geant4 simulations have also investigated the secondary electron production from GNPs. Jeynes *et al.* [42] and Martinez-Rovia *et al.* [43] have both seen slight increases in sensitization brought on by GNPs though Jeynes did not find statistically significant increases as with kV x-rays, there is still exploration to be done. The mechanism behind the potential sensitization seems to come from the ion beam reaching the high Z material (Gold), causing short range Auger electrons to be released. These short range Auger electrons will lead to the production of ROS resulting in generating greater cell death through DNA damage [42]. This phenomenon was seen to a less significant degree in the MC simulation for low energy protons (>10MeV). Ahmad *et al.* [44] have now shifted their focus on MC simulations with Geant4 to assess sensitization effects of a single GNP, to explor the enhancement effects of a "nano-film" of GNPs. They were able to corroborate that a main cause of dose enhancement was stemming from an increase in secondary electrons.

A review done by Lacomb *et al.* explores the potential of NPs and proton irradiation [20, 19, 11, 18, 36]. It is concluded that more research into the mechanism of the proton interactions in the Bragg peak region needs to be done, as utilizing NPs paired with proton irradiation does have the potential to regress the tumors and increase the radiosensitization for higher LET protons [36, 20].

One study that plays an interesting role pertaining to the proposed study is the enhancements discussed in Polf *et al.* [18]. This group ran an *in-vitro* experiment utilizing DUI45 human prostate carcinoma cells, where they constructed an experiment where the cells were treated with GNPs and irradiated with a Cobalt-60 source while the other treated cells were irradiated with a proton beam. They aimed to compare the relative biological effectiveness (RBE) for the surviving fraction of 50 % and 10 %. They used colonogenic assays to determine the survival of the cells post irradiation, finding a 15%-20% RBE increase for GNP treated cells over untreated cells [18], concluding that GNPs internalized in the prostate cells increased the ionization effects when compounded with proton irradiation.

With in-vitro experiments for the high energy protons (> 40 MeV) sensitization seems to be observed. This has been seen both in water phantom experiments [21, 44] and in-vitro experiments with a variety of of cell lines [20, 19, 18]. Unfortunately there have not been many studies for low energy protons. Those that have been executed have been with anywhere from 1 MeV to 3 MeV [36, 45], with some yielding a decrease in surviving fraction. This was observed by Liu *et al.* [45], where they looked at EMT-6 cells with PEG-gold NPs introduced and used a 3 MeV protons beam. This experiment yielded enhanced cell death, indicating it was from increased DSBs. While Li *et al.* [36] used low energy protons with an LET of 25 and 10 keV/μm paired with 5 and 10 nm GNPs. They were successful in assessing the internalization of these NPs through TEM and confocal microscopy imaging, confirming their uptake in the cytoplasm of the A431 cells. This group observed that the internalization of the GNPs within the tumor cells could produce meaningful increase in the proton dose ultimately leading to radio-sensitization effects by the GNPs.

2.5 Super Paramagnetic Iron Oxide Nano-Particles (SPIONS)

Super paramagnetic iron oxide nanoparticles (SPIONs) are said to have excellent biocompatibility [46, 47] and the potential to increase the efficiency of RT through the production of photoelectrons and Auger electrons from interactions with x-rays and γ-rays[48, 49]. Because of these potential sensistization effects, in-vitro experiments have been executed to assess the potential of SPIONs. One of the first SPION studies conducted was done by Klein *et al.* [49]. This groups utilized the MCF-7 cell line and introduced two different types of SPIONs; 0.1 mg Fe/mL of un-coated SPIONs and citrate-coated SPIONs. The irradiation was done with the use of a 120 kV x-ray tube. It was observed that an enhancement of ROS formation was present with the combination of x-ray and SPION treatments [49]. In 2017 another group looked at the potential radio-sensitization of citrate-capped SPIONs for the MCF-7 cell line as well as MDAMB-231 (human mammary gland carcinoma) and MDAH-2774 (human ovarian carcinoma) cell line [46]. This time irradiation was delivered

with a 6 MV Elekta Precise linac. They concluded that the nano-particle enhancement ratio was cell line and dose dependent, with the MCF-7 and MDAH-2774 lines observing the best results for potential sensitization at 2 Gy [46]. Current studies investigating SPION related potential sensitization [48, 46, 47, 50], have neglected exploration into PEG-coated SPIONs, therefore this functionalization on the NPs would be good to investigate.

2.6 Goals of Dissertation

This research project was designed to assess the viability of metallic nanoparticles as radiosensitizers, and more specifically the role of PEG-coated GNPs and SPIONs, paired with varying doses of proton irradiation. We aimed to establish the LD50 (lethal dose at 50%) from survival cures for the MCF7 cell line. MFC7, is a cancerous cell line of human breast epithelial cells[51]. The cells have a doubling time of approximately 29 hrs [2] and were cultured and stored in the Cell Culture Laboratory in the ECU Biology Department. The metabolic rate of the cells were assessed through use of a PrestorBlue^{TM} Cell Viability Assay. Radio-sensitization has been shown through the survival curves of the cells with PEG-coated GNPs and SPIONs incorporated with a proton beam of doses ranging from 0 Gy to 10 Gy. Each of the varying doses was also assessed with several different concentrations of PEG-coated GNPs. The use of the micro beam line in the Accelerator laboratory at ECU will provide enhanced dosimetry, and better control of the size of beam and uniformity of the beam. The ultimate goal was to assess if the concentrations of the GNPs and SPIONs paired with specific doses will allow for a greater cell death than for the cells that just receive radiation, i.e. show sensitization.

Aim 1: The first aim was to refine the existing cell irradiation experiment and narrow down specific NPs that were used. Once the project is refined and NPs were chosen the corresponding survival curves for the MFC7 line with relative doses ranging from 0 to 10 was assessed. This was done to understand what effects various doses from the proton beam

[2]found from ATCC.org under Quality control specifications for the MCF7 cell line

had on the corresponding cell line and to determine the LD50 for the line without NPs for this particular experimental set up. This is important in establishing a base line for the comparison for how the cell line will change when nano-particles are added as potential sensitizes for the MCF7 cell line.

Aim 2: The next aim was to assess potential radio-sensitization of PEG-coated GNPs and SPIONs. This was done by investigating various concentrations of GNPs combined with relative doses form 0 to 10. The goal was to understand what concentration and corresponding doses will yield the optimum radio-enhancement for the MCF7 cell line.

3 Experimental Materials and Methods

The work presented in this section was carried out for the MCF7 breast epithelial cell line for both the PEG-coated GNPs as well as the PEG-coat SPIONs. While the concentrations investigated for each NP type were slightly different, the methods for creating the dilutions and treatment of the cells was identical. Two protocols were used to set up the experiments for the custom plates and the 96-well plates. Two protocols were necessary because as the experiment was run, logistical problems with the beam energy penetrating the custom plate became apparent. The later sections in this chapter will further elaborate on the methods that are outlined in the two protocols below.

Protocol for the Custom Plate:

Day one: The experiment started with the sanitation of the custom plates, first in a 70 % alcohol bath with sonication and then in a 1 molar sodium hydroxide bath. After the second bath the plates are rinsed and assembled. Once assembled, priming media was placed in each well and left in incubation.

Day two: The priming media was removed and the plates were allowed to dry. The plates were then seeded with 10,000 cells per well and then placed back in incubation to allow the cells to adhere to the surface.

Day three: The existing growth media was removed and the desired NP concentration was placed on the cells and left in incubation for 24 hrs.

Day four: The existing growth media is removed and the presto blue (PB) assay was run for preliminary viability of the cells. Once the PB assay is complete the cells are re-dressed and brought down to the Accelerator Laboratory for irradiation. After exposure is complete the plates are placed in incubation for 24 hrs.

Day five: Twenty-four hours post irradiation the final PB assay is run on the cells to assess their viability.

Protocol for the 96-Well Plate:

Day one: The experiment started with the seeding of the 96-well plate with roughly 40,000 cells per well. Once seeded the wells were placed in incubation for roughly 24 hrs.

Day two: The desired NP concentration was achieved through serial dilution and then placed onto the respective wells. Once the NPs were placed on the cells they were placed back in incubation for 24 hrs.

Day three: The existing media is removed and the preliminary PB assay is run on the cells. Once the PB assay is complete the plates are stripped of their media and taken down to the accelerator lab for irradiation. After irradiation the cells are re-dressed with fresh media and placed in incubation for 24 hrs.

Day four: Twenty-four hours post irradiation the final PB assay is run for the cell viability.

3.1 Cell Culture and Storage

The MCF7 cell line was utilized throughout this experiment. It was made from a malignant adenocarcinoma, human breast epithelial cells. They were purchased form ATCC [52, 51] and sub-cultured in the ECU Biology Cell Culture Laboratory. The MCF7 cell line was cultured and maintained in Eagle's Minimum Essential Medium (EME) with 10 % Fetal Bovine Serum (FBS), 1 % Penicillin Streptomycin (Pen Strep), and 0.01 mg/mL of Human Incumbent Insulin, this made what was referred to as the complete growth media [52]. The excess cells that were not currently being cultured for experimental use were stored in small cryo vials in a liquid nitrogen (LN2) vat in the cell culture laboratory. Each cryo vial was stored with roughly 1 mL of cell suspension (cells mixed with pre-mixed freezing media). When ready to culture for experimental use, the cells are pulled from the liquid nitrogen. From there they are defrosted then quickly transferred into T-75 vented capped flasks where approximately 10 mL of complete growth media was thoroughly mixed to have an even dispersion of cells throughout the flask. The flask was then incubated in a Fisher Scientific incubator at 37.0 °C with 5% CO_2 for 48-72 hours or once the bottom of the T-75

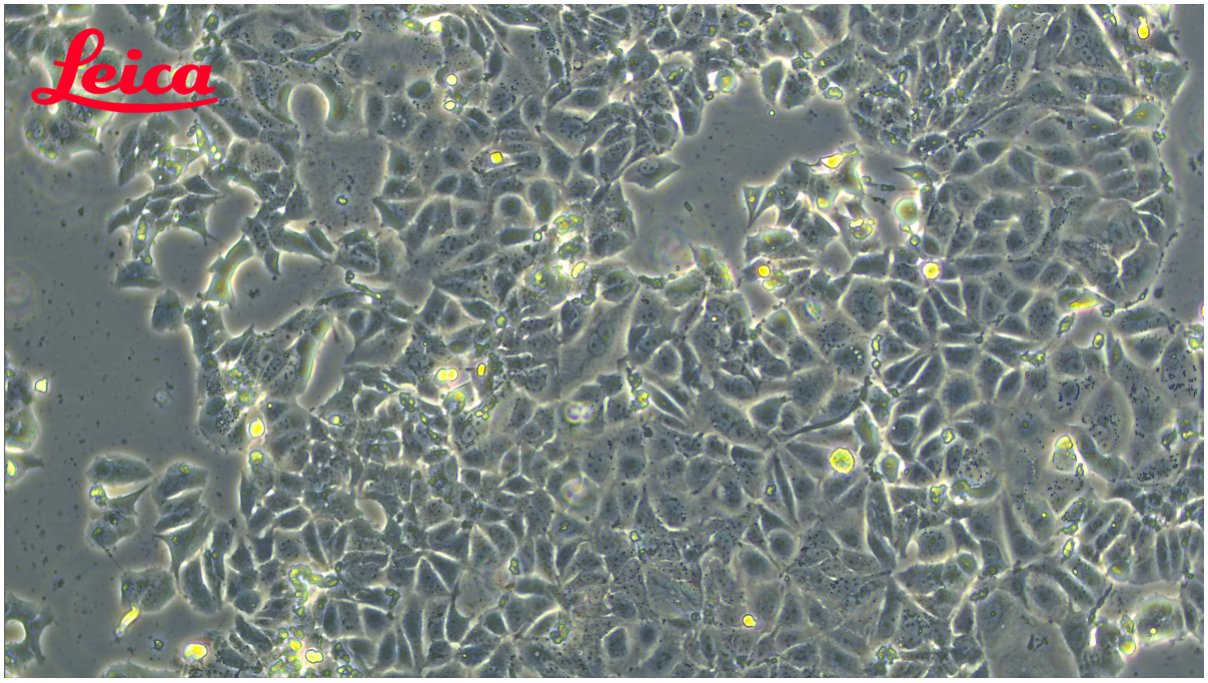

Figure 3.1: MCF7 cell line seeded in a T-75 flask, this is the typical confluency used to start an experiment. This image was done with the Leica microscopes in the cell culture lab.

flask is at least 85 % confluent which is visually confirmed through use of a microscope like seen in Figure 3.1. Once the flasks are at least 85 % confluent, the cells are removed from the bottom of the flask with 0.05% Trypsin.

To subculture the T-75 flask, the existing complete growth media was removed through use of a pipette and replaced with 5 mL of fresh 0.05% Trypsin. The Trypsin is rinsed over the layer of cells 3-5 times, then discarded. Once the first round of Trypsin is discarded 5 mL of fresh Trypsin is used to rinse the cells once more, then removed. During each rinsing process, the Trypsin is allowed to sit on the entire bottom for about 10 seconds. Once the second rinsing process is complete, the Trypsin is removed leaving a thin layer on the remaining attached cells. The flask was then put into the incubator for roughly 10 minutes or until it is visible the cells have detached from the surface under the microscope. Upon indication the cells are detached, 5-10 mL of complete growth media are place inside the flask and flushed on top of the existing cells, removing them from the bottom and thoroughly re-suspending the cells within the growth media. The cells are then ready to be re-seeded into

T-75 flasks or counted for experimental use.

If the cells were ready for experimental use the 5 mL of cell suspension from the trypsinized T-75 flask was placed into a 15mL conical where 100 μL was placed in a Eppendorf tube with 400μL of 0.4% Trypan Blue solution creating a 5:1 dilution factor. A hemocytometer[3] is then used to count the number of live cells, ultimately providing the number of viable cells within the cell suspension[53]. The cell count is then divided up into the desired wells within the plates. For the Custom plates roughly 1×10^4 cells per well were seeded while the 96-well plates had roughly 4×10^4 cells per well as they had a larger well diameter than the custom plates.

3.2 15-Well Custom Plate

Manufactured in the ECU machine shop in the physics department, a custom Acrylic 15-well plate was made to allow the low current beam to penetrate the Mylar bottom to reach the cells. The plate, pictured in Figure 3.2, shows the structure of the acrylic plate. The center plate in panel A, containing 15-wells that can hold 90 μL of cell suspension. Each well has a diameter of 4.5 mm. Roughly 1×10^4 cells are seeded into each well on a 2.5 μm thick Mylar film that has been treated with complete growth media 24 hrs prior to seeding. The treatment of the Mylar allows for a more conducive environment for the cells to attach for experimental use as the Mylar is not tissue culture treated.

A black 2.0 x 5.5 mm O-ring is used to seal the Mylar to the well creating a liquid tight seal so the cells can adhere to the Mylar. 6/32 x 3/8 inch flat Philips screws are used to seal the top and bottom plates to the center plate. Once the plate is assembled and the cell suspension is seeded into each well, the plates are moved in a circular motion on a flat surface to help create even dispersion of the cells. This motion is key for the creation of a mono-layer of cells adhered to the Mylar film. It is important to achieve a mono-layer of cells for the purpose of uniform irradiation. Before irradiation the plates are then set in the

[3]the linked site provided the process for counting cells; https://www.abcam.com/protocols/counting-cells-using-a-hemocytometer

incubator at 37.0 °C and at 5% CO_2 for 24 - 48 hrs.

One concern is the potential of contamination because the plates are re-usable. To deal with potential contamination, the plates are first soaked in 70% alcohol with sonication for 30 minutes. This is done to knock any potential contamination out of all crevices of the custom plates. Once the alcohol/sonication bath is complete the plates are rinsed and put into a bath of 1 molar solution of sodium hydroxide for 45-65 minutes. They are then rinsed several times with sterilized deionized water and set to dry for 10-15 minutes in a hood before the assembly occurs.

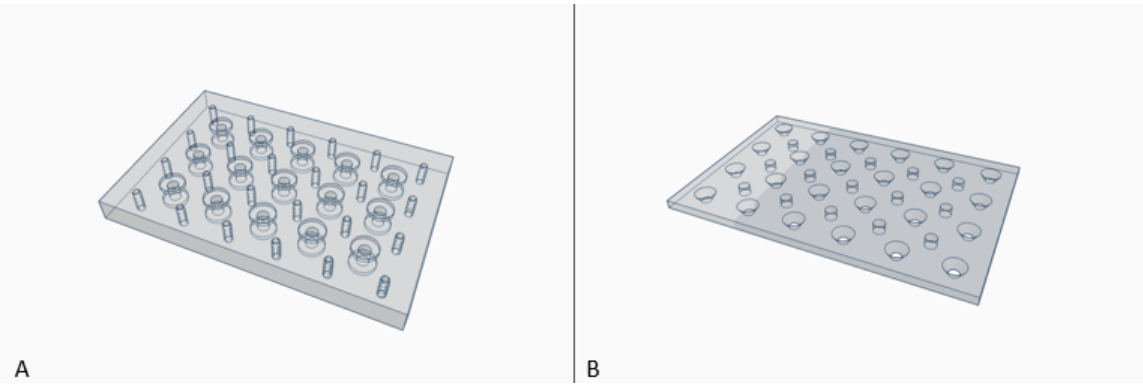

Figure 3.2: This figure displays the parts to the cell culture plates that were made specifically for this experiment. Figure A shows the center plate where the Mylar film will be placed on the top and bottom with o-rings securing the Mylar in place, Figure B is the top and bottom plate that will compress the o-ring making it leak proof, and then the top and bottom plate will be screwed in to maintain the seal.

3.3 96-Well Corning Plate

To understand if the cells were receiving the proper dose on the custom well plates, the same experiment was also run on 96-well plates to assure proper dose deposition was happening. These plates were sterile, flat bottom 96-well plates that have been tissue culture treated for optimal set up to generate a mono-layer of cells. Of the 96-wells only 24 were seeded, with roughly 40,000 cells per well. The configuration is displayed in Figure 3.3. The blue wells are the wells that were seeded with cells while the white wells remained empty. This configuration was chosen to allow no single exposure to overlap, i.e. there is at least

one skipped well between each sample assuring single exposure to the cells in the blue wells. The set up also allowed for less use of the mechanical stage (section 4.5) by utilizing the symmetry of the 96-well plates, ultimately cutting down on how long the plates are out of incubation. When irradiating the plates each set of plates will have 1-2 control plates that are subjected to the same environmental changes as the irradiated plates to account for any in air contamination or death that would happen. It is important to note that the 96-well plates were brought down to the accelerator lab with no media on the cells for irradiation. This means time is of the essence as cells that are left without media for too long will tend to die as they are in an inhospitable environment. The process of seeding started with the counting of the cells from the T-75 flask outlined in section 3.1, and ultimately concluded with each well having roughly 45,000 cells per well. This cell count allowed for a roughly 80% confluency on the bottom.

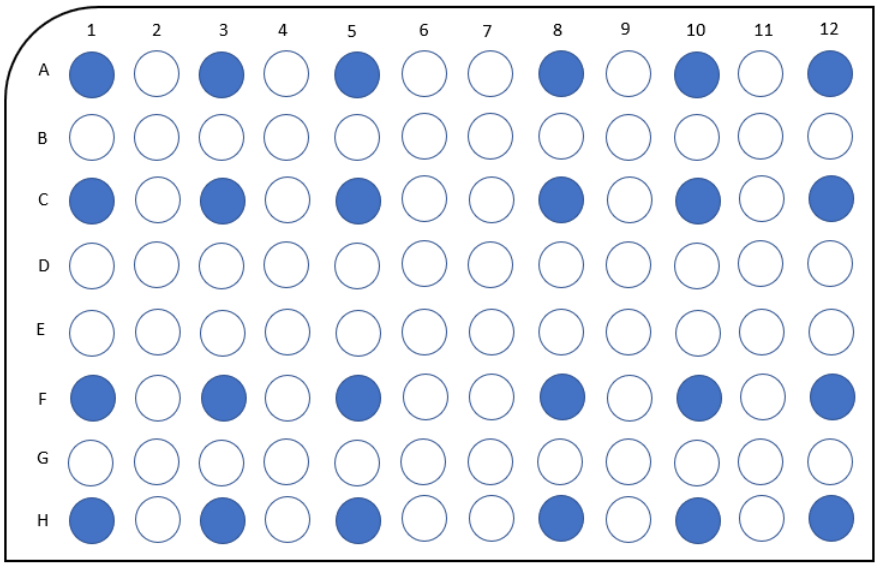

Figure 3.3: This figure shows how the 96-well plate is seeded for irradiation. The blue filled circles are the wells that are seeded while the white circles remain empty.

3.4 Type of NPs and their Incorporation

There were two types of NPs utilized for the experiment; PEG-coated GNPs and PEG-coated SPIONs. Both NP types were spherical in shape, and coated with PEG to help enhance compatibility and cellular uptake.

The PEG-coated GNPs were purchased from Sigma-Aldrich in 1 mL vials of 136 nM concentrations suspended in water. Their diameter was averaged to be 15 nm, but ranged from 13-17 nm. This particular size was chosen from the literature implying PEG-coated GNPs yield sensitization effects best between the 5-30 nm range [29, 30, 39]. The GNPs were functionalized with amine and a PEG coating with a molecular weight of 5000 which helps prevent aggregation of the GNPs [54, 33]. While the GNPs themselves have a molecular weight of 18.02 g/mol [55].

The PEG-coated SPIONs, were also purchased form Sigma-Aldrich in 10 mL vials of high concentrations by a collaborating lab at ECU. The average diameter size of the SPIONs ranged from 28-32 nm [56], giving them an average diameter of 30 nm. From the 10 mL vials the SPIONs were coated with PEG on the Brody School of Medicine Campus in the Beltran-Huarac Lab and placed into 1 mL vials of 5 μg/mL, which gave a concentration of 21,600 nM to start.

For both NP types a serial dilution was run from their respective starting concentrations. For consistency's sake the dilutions were mirrored, but because of the higher starting concentration of the SPIONs (21,600 nM), larger concentrations were explored. For the GNPs, their starting concentration was 136 nM per 1 mL vial, the concentrations explored were 34 nM for the custom plate experiments and 68, 45, and 15 nM for the 96-well plate experiments. While the SPIONs starting concentration was 21,600 nM, which allowed for concentrations of 136, 45, and 15 nM to be tested.

The serial dilution for each NP type is pictured in the Figures 3.4 and 3.5, showing how to get the exact concentrations. Equation 5 below was utilized to find each of the

concentrations.

$$M_1V_1 = M_2V_2 \tag{8}$$

Where M_1 is the starting concentration (nM) and V_1 is the starting volume of solution (mL), and M_2 is the final concentration (nM) and V_2 is the final volume of the solution (mL). For each NP type a portion of the starting concentration was taken and diluted with the complete growth media of the MCF7 cell line and placed into the first conical labeled A. For the PEG-coated GNPs this meant a first concentration of 68 nM suspended in 4 mL of media. While the PEG-coated SPIONs had a final volume of 19 mL with a concentration of 136 nM. The next conical labeled B will hold the second largest concentration; 45 nM for both the GNPs and SPIONs, with a final volume of 2 and 18.5 mL respectively. This was done by taking a portion of larger concentration from conical A, and then diluting with complete growth media. The smallest concentration was made in the conical labeled C by taking a fraction of the 45 nM concentration from conical B and then diluting it with a specific amount of growth media (shown in Figures 3.4 and 3.5). Once the dilutions are complete the 3 conicals are used to distribute 100 μL of the NPs solution to the desired wells. This was done by removing the existing media over the cells and replacing with the 100 μL solution of the desired concentration. Once the NP solution has been placed on the wells, they are placed back in incubation for roughly 24 hrs, to allow the NPs to integrate into the mono-layer of cells on the base of the plate [39, 57]

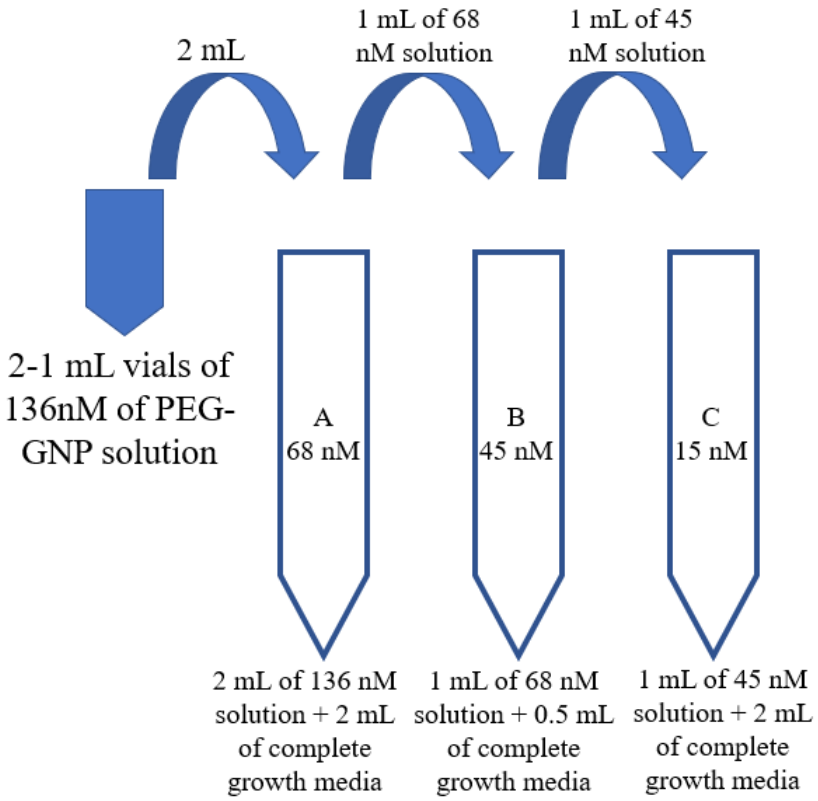

Figure 3.4: This figure shows the serial dilution used to obtain the PEG-coated GNP concentrations.

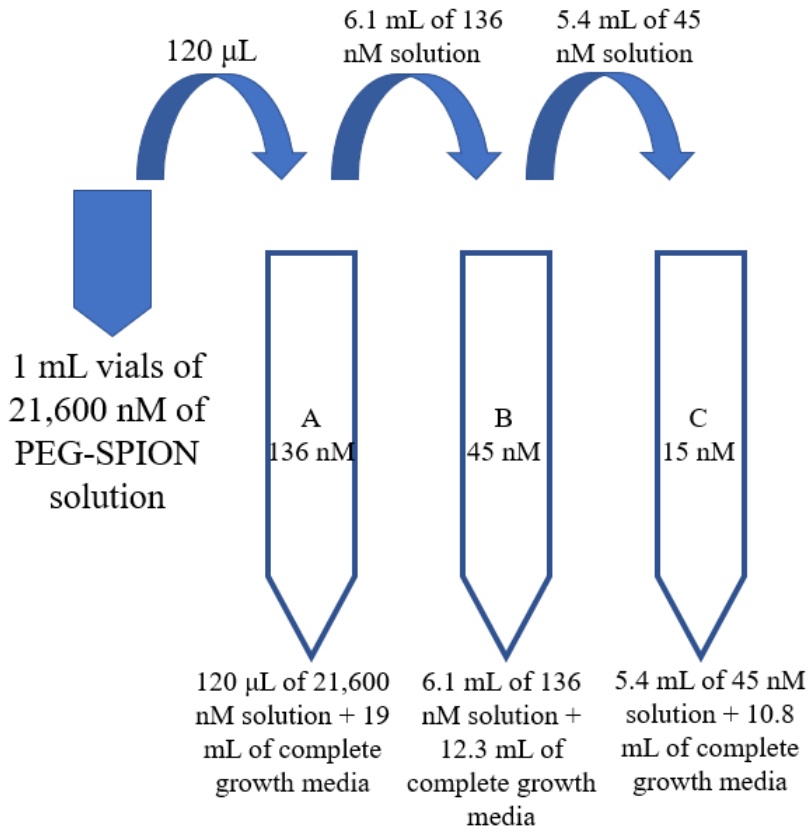

Figure 3.5: This figure shows the serial dilution used to obtain the PEG-coated SPION concentrations.

3.5 2MV Tandem Pelletron Accelerator

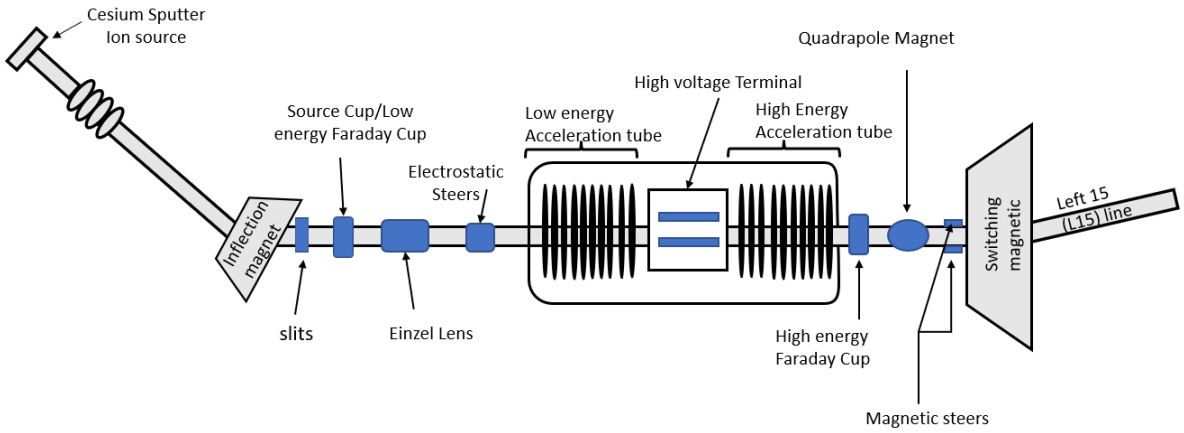

Figure 3.6: Schematic of the ECU 2MV Electrostatic Pelletron Accelerator

The ECU Accelerator Laboratory houses a 2MV Tandem Electrostatic Pelletron Accelerator that was commissioned by the National Electrostatic Corporation (NEC), model 6SDH-2. The accelerator being a 2 MV tandem particle accelerator, means when conditioned to its maximum energy for hydrogen ions, it has the potential to get to energies as high as 4 MeV. The 4 MeV is possible, as the charge on the terminal roughly translates as MeV=$q*2$, where q is the charge. For the purpose of this experiment a 1.482 MV beam that translates to a 3 MeV proton beam was used.

In Figure 3.6, the accelerator is broken up into 3 major sections. The first is the source side, which encompasses everything from the cesium ion sputter source to the first Faraday Cup (FC); the source cup. This section is where the beam will be initially generated. The second and third major sections are separated by a high voltage terminal where the major production of the accelerated ion beam occurs. The second section is referred to as the low energy (LE) side. The LE side extends from the inflection magnet to the high voltage terminal. Downstream of the high voltage terminal is the third major section referred to as the high energy (HE) side. The HE side extends from the high voltage terminal to the switching/analyzing magnet [58]. The purpose of the FCs is monitoring the current of the beam, manipulating its shape, and blocking the beam. Each cup has an "in" and "out" position. When the FC is in the "in" position it is able to read out the current on the software at the control station while simultaneously blocking the beam from traveling farther down the accelerator beam tube. When the beam is in the center of the FC it will read out its maximum current; this current can be found by shaping and focusing the beam through the lenses and magnets that are before each respective cup. When the maximum current is measured it implies the beam is aligned perfectly in the center of the accelerator beam tube. This center alignment allows better fine tuning of the beam shape and size for experimental use.

3.6 Generating a Beam

To start the process of generating an ion beam the cesium sputter ion source (Figure 3.5), needs to be warmed up to roughly 120 degrees Celsius, (but can be maintained at a higher or lower temperature, as needed for other experiments). As the oven temperature increases, positively charged cesium ion (Cs^+) vapor is produced. It is important to note that the Cs^+ vapor is an excellent electron donor and will play a key role in the creation of the proton beam for this experiment. The Cs^+ are drawn toward the negatively charged cathode comprised of titanium hydride (TiH). When the Cs^+ interact with the electric field of the TiH, atoms will be sputtered off the cathode and the Cs^+ will donate an electron and create negative hydrogen ions (H^-), thus starting the initial process of making a proton beam. The H^- are drawn down toward the terminal where they are bent toward the accelerator beam tube. The beam is then steered and focused by the Einzel lens and Electrostatic Steers toward the accelerator tank on the LE side of the tank [58, 59].

In order to produce the desired energy for the experiment and start the first of the two acceleration processes, the NEC software was used to turn on the pellet chains located on the HE side of the accelerator. The pellet chains, are made up of alternating metallic and insulating connections. These chains are what will effectively "dump" energy onto the high voltage terminal [60]. The high voltage terminal is positively charged attracting the H^-, where they will enter the "stripper" in the center of the high voltage terminal. While in the "stripper" the H^- are exposed to nitrogen gas (N_2). The N_2 will strip the H^- of its electrons, converting them into protons (H^+), thus creating the proton beam. H^+ are repelled by the positively charged high voltage terminal, generating the second acceleration process which moves the ions from a charge state of +n to a final energy of (n+1) eV [58] providing twice the initial energy of the beam.

As the particles are accelerated out of the tank and through the accelerator beam tube, there are a series of lenses and magnets in place to focus and steer the beam. The first thing the beam encounters when exiting the accelerator tank, is the HE FC (Figure 3.6)

As previously discussed the FC can be used as a beam blocker, but more importantly it can be used to focus the beam down the center of the accelerator beam tube, by finding the maximum current on the cup. Once current is maximized on the HE FC the analyzing magnet, through a momentum selection process, bends the protons 15 degrees into the L15 beam line.

3.7 Accelerator Beam Line L15

The L15 beam line also known as the micro beam line, was utilized for the cell irradiation experiment. The line was designed with features to be able to collimate via the slits (pictured in Figure 3.7) to adjust the beam down to micrometer diameters. The line is fit with several features to optimize the functionality of the line. The first important feature on the line is the NEC fast valve. This is located right after the switching magnetic, and with the pressure sensor located at the end of the line near the Havar metal alloy exit window (Pictured in Figure 3.7). The Havar exit window is only 0.001 cm thick and if perforated it would flood the line with air, bringing the pressure (10^{-8} torr) up to atmosphere almost instantly, causing catastrophic damage to the accelerator. As a preventative measure, the pressure sensor would be tripped, slamming the fast valve shut, effectively cutting the L15 line off from the rest of the accelerator.

The next feature on the beam line are the slits. These slits are used to collimate the beam and, can also be used to minimize the beam current, which is critical for this experiment. The first of the two FCs are next on the line. The first Faraday cup is attached to the line by a cross conflat piece, and used to measure the current of the beam. This FC is also utilized to monitor any fluctuation in the beam current throughout the experiment. On the bottom of the cross piece is the turbo molecular pump and below that attached by a foreline is a rough pump. The turbo pump and rough pump are what brings the L15 line down to the desired pressure (roughly 3×10^{-8} torr). The Faraday cup above both pumps, when placed in the center of the line in the "in" position reads out the current. This current is what is key

to generating exposure times for specific doses and will be further explored in the following dosimetry section. After the FC, are a set of x and y magnetic steers. These steers function to move the beam left/ right and up/ down. Downstream to the magnetic steers, is a beam profile monitor (BPM). The BPM is hooked up to an oscilloscope stationed at the control desk. The BPM allows for beam shape and uniformity to be monitored. Finally, after the BPM there is one last, important Faraday cup right before the Havar exit window. While this cup is not used to measure current, it is programmed via LabView to block the beam at programmed intervals to receive the desired exposure time to the cells lined up with the exit window (Figure 3.8)

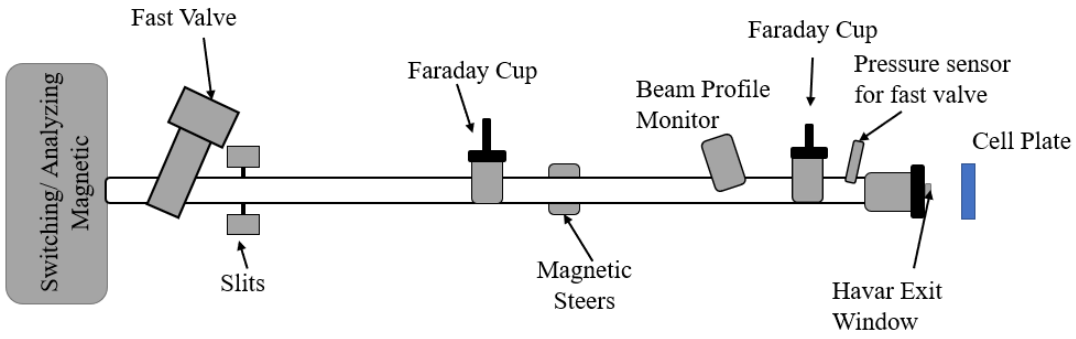

Figure 3.7: Schematic of the L15 Micro Beam line in the ECU Accelerator Laboratory.

At the end of the line, is the Havar exit window, 17mm away from the exit window is the mechanical stage, which had two different holders that can be mounted on it. One to hold either the custom or 96-well plate and another with a cerium-doped yttrium aluminum garnet (YAG) crystal inserted within the center of a custom plate (Figure 3.8). The crystal is lined up by way of a New England affiliated technologies (NEAT) stage. This stage is motorized allowing precise use of the full plate whether it be the custom or 96-well plate. Behind the YAG crystal is a camera lined up and feeding a live image to the beam line computer. The beam will be steered down the L15 line by use of the switching magnet.

Where it will be spread out to achieve a uniform beam by using the quadrapole magnet (Figure 3.6), by adjusting the strength and balance settings. Uniformity of the beam can be assessed first by lining the beam up on the YAG crystal. When the beam is aligned on the crystal it will illuminate the crystal, allowing the camera to pick up a visual of the beam and its intensity. The camera (Figure 3.8) is used to image the beam. The images taken by the camera are used to measure the uniformity of the beam (Figure 3.8 top right and bottom right panels) and to the measure the beam size via ImageJ software.

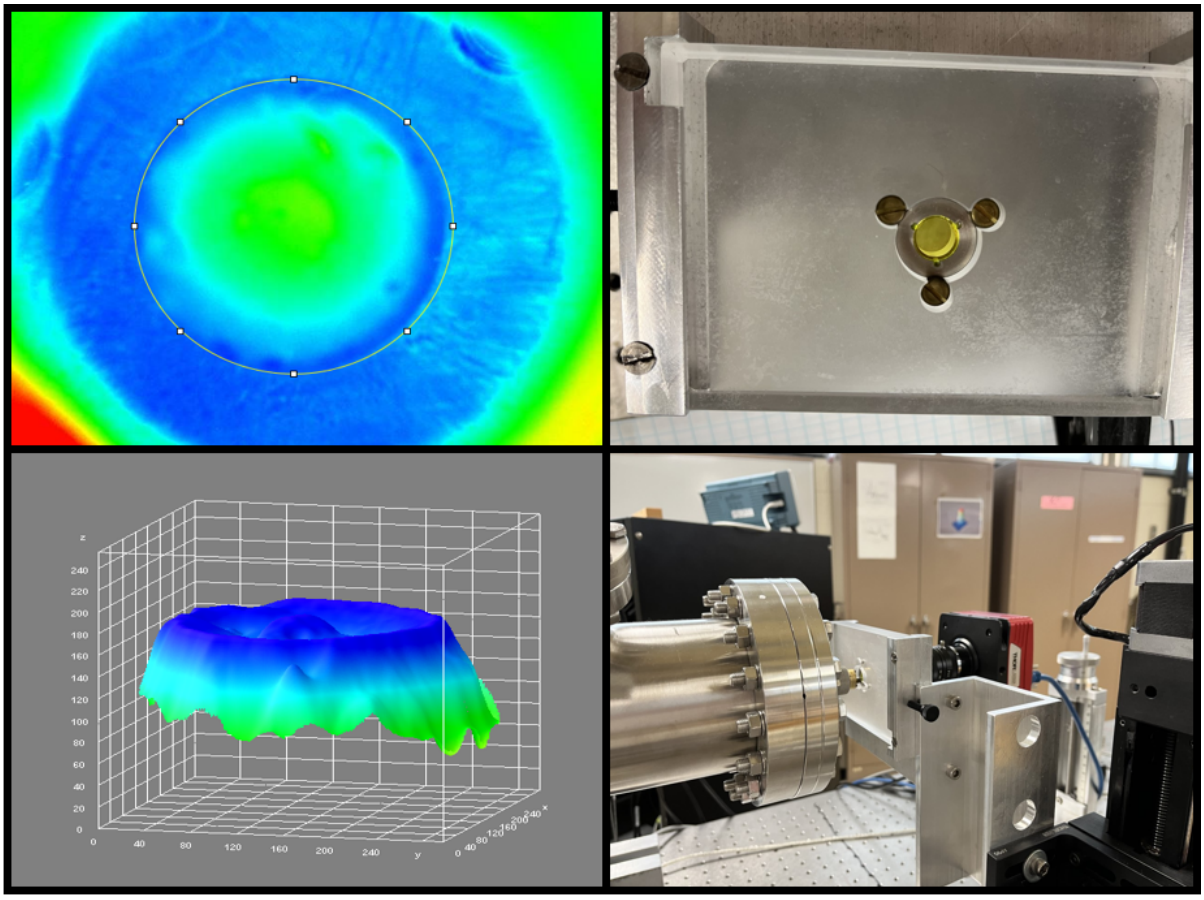

Figure 3.8: The four panel image shows the YAG crystal in the top right and bottom left. When the beam hits the crystal the camera will show the beam spot (top left) and ImageJ was used to create a surface plot of what the beam spot looks like (top and bottom left).

The beam is measured to roughly 5 mm, which is the diameter of the 96-well plate and roughly 0.5 mm larger than the custom plate, and uniformity is achieved within the limits of this experimental design. The current is monitored and doses achievable for that experiment

can then be assessed.

3.8 Cell Irradiation and Dosimetry

As previously outlined, the MCF7 cell line was irradiated on the L15 beam line by a 3 MeV proton beam. In order to estimate the dosimetry, several parameters needed to be explored based off the experimental set ups. First the energy lost at the Havar exit window needed to be understood, along with the distance the beam travels through air and, what materials the beam must penetrate to irradiate the cells, i.e. the Mylar and layer of cells for the custom plate experiments and just air for the 96-well plates. To start the dosimetry calculations, the first step is to determine the mass stopping power ($\frac{dE}{\rho dx}$) [4] of the 3 MeV proton beam. This is done by utilizing The Stopping and Range of Ions in matter (SRIM) and Transport of ions in Matter (TRIM). This code allowed input of a material at various beam energies to achieve the materials mass stopping power as well as simulate the ions trajectory and energy deposition [61]. Once the mass stopping power is determined the LET of the Havar foil was determined through equation 6, where $\frac{dE}{\rho dx}$ is the mass stopping power from the SRIM code (MeVcm^2/mg) and ρ is the density of the Havar foil (mg/cm^3). The LET for the beam in air as well as through the Mylar and cells needed to be found using the same process. These numbers were found for the custom plate experiment as well as the air and cells for the 96-well plates as the distances the beam will travel in air were different. All of these values are displayed in tables 2 and 3. Once the LET was found the energy loss of the beam through all of the materials can be found by subtracting the starting beam energy (3Mev) from the individual energy losses (equation 7). Next the energy at the cells was found ($E_{remaining}$), it was used to find the mass stopping power, giving the variables needed to find the dose rate ($\dot{D}$, equation 8). Finally the fluence rate ($\dot{\phi}$), was found using equation 9. Fluence rate is current (I) dependent, which is the current produced in the L15 beam line measured by the first FC. Once the dose rate was calculated the exposure time was calculated, using the desired dose (D) divided by the dose rate. It is important to note that

the exposure times were current dependent; if a high exposure rate is desired (> 3 seconds), a low current (typically < 7 nA) was needed to explore a wide range of doses.

The calculations for doses that were used experimentally were obtained through the numbers calculated from SRIM and the beam current, which would typically reflect a unit of Gray (Gy). however as they were obtained from a theoretical energy loss and not verified experimentally they are described as a "relative dose" with no dimension. This notation will be carried on throughout the results and discussion sections.

$$LET = \frac{dE}{\rho dx} \times \rho \tag{9}$$

$$E_{remaining} = E_0 - E_{loss} \rightarrow E_{loss} = LET \times d \tag{10}$$

$$\dot{D} = \dot{\phi}(\frac{dE}{\rho dx}) \tag{11}$$

$$\dot{\phi} = \frac{I}{AQ} \tag{12}$$

Material	LET ($\frac{MeV}{cm}$)	Density ($\frac{mg}{cm^3}$)	Thickness (cm)
Havar	547.95	8.3×10^3	0.001
Air	0.1645	1.63	2.4
Mylar	0.1417	1.40×10^3	0.00025
Cells	170.04	1090	0.0025

Table 2: Shows the materials and their respective LET, density and thicknesses for the custom plate experiments.

Material	LET ($\frac{MeV}{mm}$)	Density ($\frac{mg}{cm^3}$)	Thickness (mm)
Havar	53.950	8300	0.01
Air	0.019	1.21	17
Cells	61.991	1.09	0.0025

Table 3: Shows the materials and their respective LET, density and thickness for the 96-well plate experiments

3.9 Cell Viability

In order to quantify cell survival, a cell viability assay is run. The cell viability was related to the metabolic rate of the cells via a PrestoBlue^{TM} assay, which was purchased form Thermo Fisher Scientific. The PrestoBlue solution is made of a resazurin-based reagent that will interact with the viable cells to produce a color change based on the metabolic rate of the cells [62]. This color-metric assay was chosen for its ease in experimentation, as well as the cell viability after the assay, allowing this assay to be run multiple times on the same set of cells, as opposed to an endpoint assay like MTT [62].

The assay began by taking the PrestoBlue^{TM} viability reagent and mixing it with the complete growth media of the MCF7 cell line (described in section 4.1). It was a 1:10 ratio, 90% complete growth media to 10% PrestoBlue solution. This mixture was mixed the morning it was utilized. The morning of irradiation, the existing growth media in each well was removed and the cells were rinsed with PBS then 100 μL (for the 96-well plates) and 90 μL (for custom plates) of the PrestoBlue mixture was placed over the cells. It is important to note that this assay is sensitive to light and was preformed in a semi-dark lab and the plates were covered with foil to protect the PrestoBlue solution from degrading. Once the mixture is placed on all of the plates, they were incubated for 2hrs. The time is determined based off of linearity testing. The more confluent the wells are the less time is needed in the incubator. Highly populated wells will tend to saturate after 3 hrs for the MCF7 cell line and using a linearity test can help understand at what time frame this can occur for specific cell densities.

Following the 2 hr incubation period, the PrestoBlue mixture was removed from the cells and placed into a fresh 96-well plate along with a control column of complete growth media as see in Figure 3.9, and stored in the incubator until all the plates had been irradiated.

Once all of the plates have been stripped of their PrestoBlue mixture, the custom plates were then replaced with fresh complete growth media and their plates assembled. While the 96-well plates were left with no media. Both were then transported to the accelerator lab for irradiation (as covered in sections 3.5 & 3.6). As mentioned before, post irradiation the plates are dressed (96-well plates) and placed back in incubation. At that point the plates with the PrestoBlue mixture were taken to the Thermo Scientific Multiskan FC plate reader to measure the absorbance levels at 570 nm and 620 nm [63, 64]. The color change of the PrestoBlue reagent will depend on the number of viable cells, the more fuchsia the color, the more densely populated the well is with viable cells. When evaluating the absorbance number, a control well was used to correct for background noise; the control (C) is the complete growth media that is used in the assay. To analyze the data the difference between the two absorbance values for each plate were taken into account (570 nm - 620 nm). This processes of cell viability was also run 24 hrs post irradiation. This was done to have a pre (t_0) and post (t_1) set of data to compare to ultimately find surviving fractions. The control absorbance values needed to be averaged across each plate for that run, this average was then be subtracted out of each pre (t_0) and post (t_1) values. Once the control data was accounted for each t_0 absorbance value for each trial were then averaged, likewise for t_1, this left 2 variations of t_{1av}, the irradiated (t'_{1av}) for each specific dose and NP concentration and non-irradiated (t_{1av}) for each NP concentration and vice versa for the t_{0av}. Once the two were distinguished, the fold was found, which resulted in a comparison of the average absorbance before and after irradiation (equations 13 and 14)[64].

$$F = t_{1av}/t_{0av} \tag{13}$$

$$F' = t'_{1av}/t_{0av} \tag{14}$$

The two-fold numbers represented the comparison of the irradiated wells (equation 13, F') and the non-irradiated wells (equation 10, F). To normalize the irradiated cells, F' was divided by F. This provided a surviving percentage of cells from the experiment. Once the surviving percentage was achieved, the percentage was plotted against the relative doses to get the survival curve. The survival percentages were examined graphically and used to quantify the sensitization enhancement ratio (SER)(equation 15). Where the subscript D of equation 15 is the dose for that fraction and C is the concentration for that same dose.

$$\mathrm{SER} = \frac{\mathrm{Survivingfraction_D}}{\mathrm{Survivingfraction_{D,C}}} \tag{15}$$

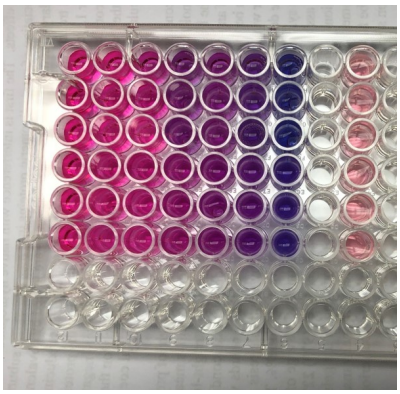

Figure 3.9: The image shows the color change achieved after 2hrs of 90 μL of a 1:10 Presto-Blue to complete growth media ratio. From right to left reflects the highest cell count per well (100,000 cells) to the lowest count 10,000 cells per well.

3.10 SRIM and TRIM Applications

The SRIM code as previously stated in section 4.6 is a powerful tool that will allow the user to obtain a particular ion's projected range, and stopping power (Figure 3.11) through a pre-determined material in the compound dictionary. Figure 3.10 shows an example of Hydrogen ions passing through a target material (Havar), at various energies and what the

particular stopping power the ion would yield based off the target material [61]. These numbers were key in the dosimetry as covered in section 4.6. Another feature of the SRIM applications is the TRIM code, which is a Monte Carlo simulation that allows the input of a particular ion at a specific energy and simulates the ion's trajectory through whatever desired materials (Figure 3.11). This simulation was key to projecting how the proton beam should move through various experimental setups and how the beam deposited its energy.

The first use of SRIM in this experiment was to project the energy loss in each material the proton beam would travel through. This aided in the exposure time calculations to the cells in air (96-well plates) and with the custom plates. Both indicated there would be energy left over to irradiate the cells, which was ultimately used to estimate the dosimetry for this experiment. The next step was to simulate these phenomena utilizing TRIM. The figures that can be derived from the Monte Carlo simulations show the proton beams projected path and expected energy loss as the beam travels through the various materials for both experimental set ups. The SRIM and TRIM interfaces both are equipped with a vast pre-made materials list. For this experiment both were used in the assessment of the experimental set up and well as to trouble-shoot inconsistencies in the experimental results. When initially using SRIM calculated energy loss implied both set ups would have energy deposited to the mono-layer of cells. Because of that both experimental set ups were tested and will be discussed in in their respective results sections in Chapter 4.

Ion = Hydrogen [1] , Mass = 1.008 amu

Target Density = 8.3000E+00 g/cm3 = 8.6304E+22 atoms/cm3

======= Target Composition ========

Atom Name	Atom Numb	Atomic Percent	Mass Percent
C	6	000.96	000.20
Cr	24	022.29	020.01
Mn	25	001.69	001.60
Fe	26	018.11	017.47
Co	27	041.78	042.52
Ni	28	012.83	013.00
Mo	42	001.45	002.40
W	74	000.88	002.79

==========

Bragg Correction = 0.00%

Stopping Units = MeV / mm

See bottom of Table for other Stopping units

Ion Energy	dE/dx Elec.	dE/dx Nuclear	Projected Range	Longitudinal Straggling	Lateral Straggling
2.00 MeV	6.992E+01	4.675E-02	18.21 um	9372 A	1.47 um
2.25 MeV	6.495E+01	4.229E-02	21.88 um	1.14 um	1.73 um
2.50 MeV	6.073E+01	3.866E-02	25.81 um	1.34 um	2.01 um
2.75 MeV	5.711E+01	3.564E-02	30.01 um	1.54 um	2.30 um
3.00 MeV	5.395E+01	3.308E-02	34.46 um	1.75 um	2.61 um

Multiply Stopping by	for Stopping Units
1.0000E-01	eV / Angstrom
1.0000E+00	keV / micron
1.0000E+00	MeV / mm
1.2049E-03	keV / (ug/cm2)
1.2049E-03	MeV / (mg/cm2)
1.2049E+00	keV / (mg/cm2)
1.1587E-01	eV / (1E15 atoms/cm2)
9.4551E-02	L.S.S. reduced units

==========

Figure 3.10: This figure shows the output of the SRIM software and what kind of information can be generated.

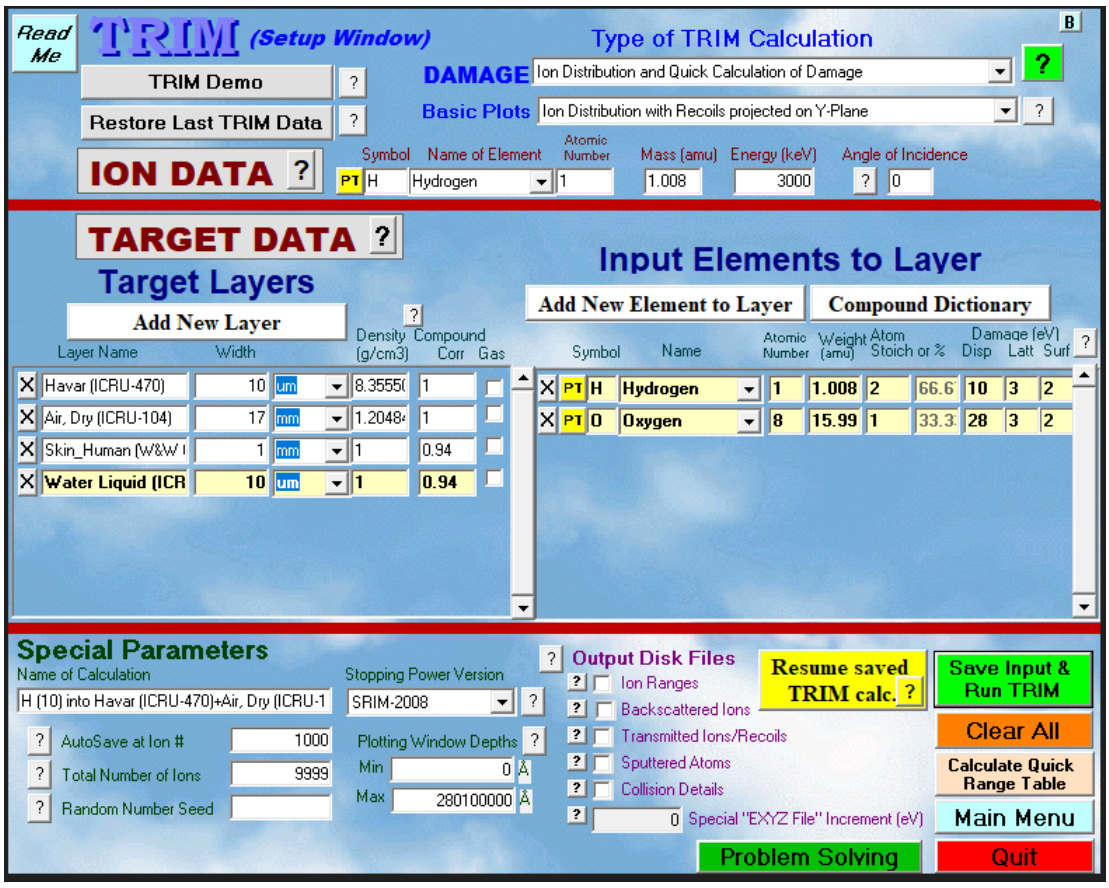

Figure 3.11: This figure shows the interface for inputting the layers needed to test an experimental set up.

3.11 Statistical Analysis

For the statistical analysis the significance between the non-treated cells to the treated cells was analyzed through the use of R Studio version 4.0.5. The data was compiled into an excel spread sheet, where R could run comparisons between the non-treated cells for each relative dose to each concentration of NPs for that same relative dose. These data were assessed for normality using a Shapiro-Wilk Normality Test [65]. This test assumes a normal distribution of data, with an analyzed p-value of 0.05 or less resulting in rejection of the null hypothesis and data being considered not normally distributed. Most of the data sets were determined to be normally distributed, however there were 5 sets that were not normally distributed, a Wilcox test was run to obtain the p-value for statistical significance

($p < 0.05$). For the data that was normally distributed, a Student's t-test was used. In order to use that particular t-test, it needed to be stated if the variances between the two samples were equal or unequal, so a variance test between each compared set was done. Once that was determined each set of data for each relative dose could be compared and tested for significance. The data set was accepted as statistically significant if the decrease in surviving fraction yielded a p-value less than 0.05.

4 Results For MCF7

4.1 Standard Curve Testing

Linearity, also known as standard curve testing, is an important starting base when using prestoBlue. Through the linearity testing done for the MCF7 cell line, 4 standard curves were made at 4 different time intervals to find the optimal incubation time (Figure 4.1). Utilizing the prestoBlue reagent, and complete growth media for the MCF7 cell line, the two are plated and then run through a 96-well plate reader and analyzed as described in the Cell Viability section, 3.9. The time frames examined included: 0.75 hrs, 1.5 hrs, 2 hrs and 3.5 hrs. The plates were examined colorimetrically by a plate reader to assess meaningful color change (indigo to fuchsia), and when saturation became apparent on the wells as seen in Figure 4.2 on the bottom right panel.

For the in-air 96-well plate experiments, roughly 40,000 cells per well were seeded to achieve the desired confluency within the 96-well plates. With that in mind the linearity plates were seeded with 7 different columns of 120,000, 96,000, 78,000, 60,000, 48,000, 36,000 and finally 12,000 cells per well. The plates were seeded and incubated identically to the plates for the irradiation experiment. Figure 4.1 shows the color change for each plate after their respective incubation period. The top left panel was pictured and run after 0.75 hrs in incubation, top right was 1.5 hrs, bottom left, 2 hrs and bottom right, 3.5 hrs. It can be noted that on all of the plates the fifth column from the left is the column was seeded with 48,000 cells per well, while the sixth column that was seeded with roughly 35,000 cell per well. The experimental count fell in between the two making them the columns of interest. For the first two time frames 45 minutes and 1.5 hrs, none of the wells produced saturation, which can be seen in Figure 4.1. When the color starts to saturate the standard curves will no longer produce a linear trend. In Figure 4.2 it can be seen that the 0.75 hrs and 1.5 hr time frames both produce a relative linear trend for all cell counts. At the 2 hr time frame (top left panel), it can be seen that the trend starts out linear and transitions

into exponential growth, showing that the cell counts above 48,000 cells per well have been left in incubation too long, rendering absorbance values above 48,000 cells inconclusive and excluded as a possible time frame for this experiment. This trend is also observed at the 3.5 hr mark after 36,000 cells per well. These results helped guide the experiment to a 2 hr incubation time for the experimental cell count as it yielded meaningful color change visually, but also did not indicate saturation on the standard curve.

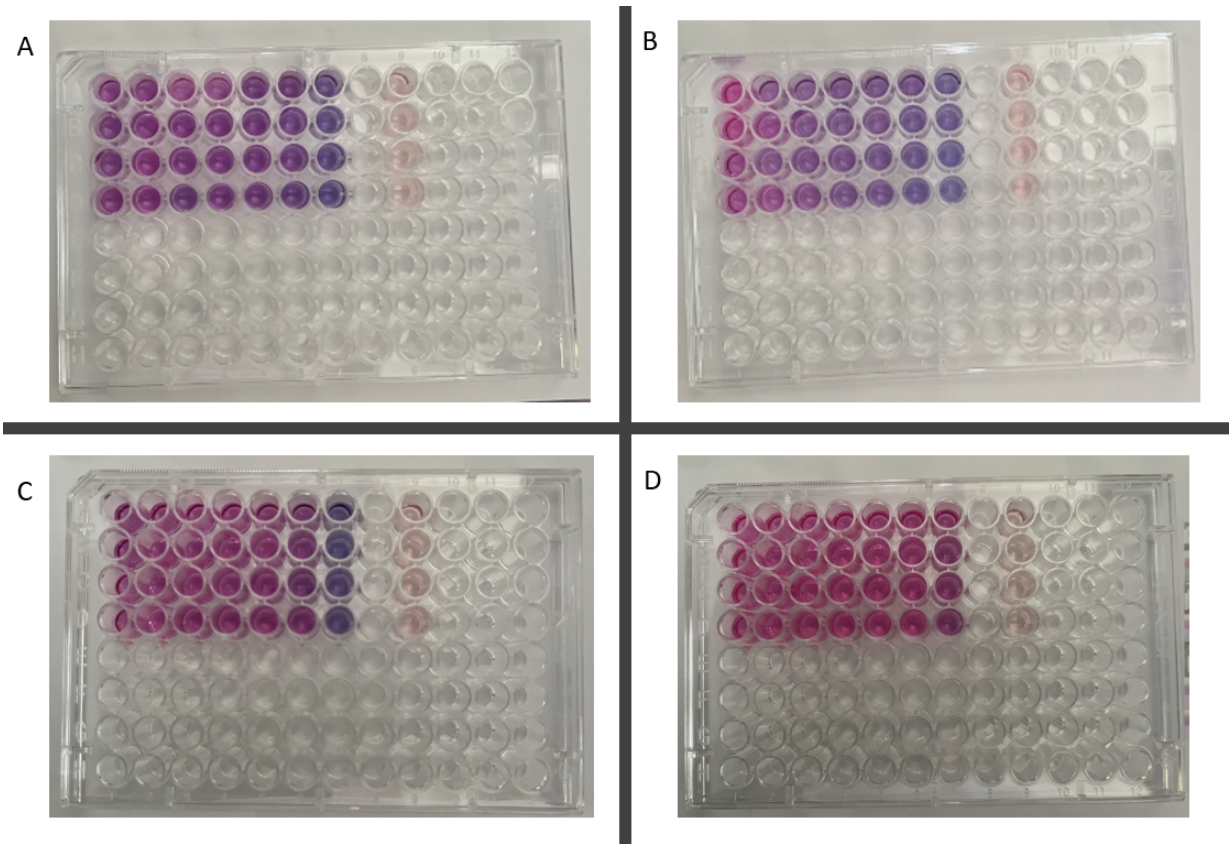

Figure 4.1: The four panels represent the color change at different time intervals, A is at time interval 0.75 hrs, B is 1.5 hrs, C is 2 hrs and D is 3.5 hrs. They are all seeded with the same number of cells the left column having around 120,000 cells and the far right having around 12,000 cells.

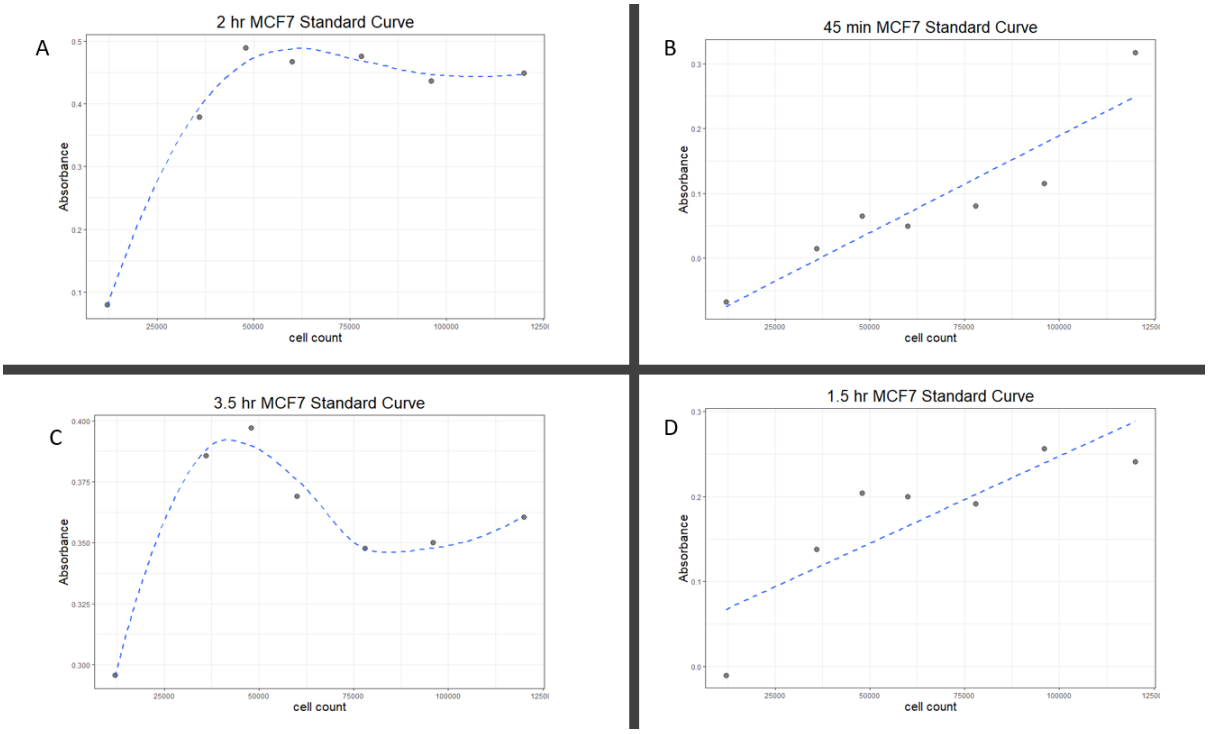

Figure 4.2: The absorbance values at 550 nm and 620 nm and are graphed against the number of cells per well. Panel A is the 2 hr time frame, B is the 0.75 hrs, C is the 3.5 hrs and D is the 1.5 hrs.

4.2 Custom Plate Survival Curve and Sensitization Effects

The custom plate experiment was the first iteration of this experiment to be executed on the micro-beam line. The custom plates were set up one at a time on the mechanical stage at a distance of 24 mm from the Havar exit window. Figure 4.3 shows the survival of the MCF7 cell line before the addition of any NPs. This is an important plot to determine the MCF7 cells baseline reaction to the 3 MeV proton beam. it is important to reiterate that the doses were not experimentally confirmed. They were determined through the use of SRIM LET data (as discussed in section 3.8), yielding a dose in Gray (Gy). Because they were only theoretically calculated the doses presented throughout are referred to as relative doses rather than "dose" with no dimension as opposed to the standard Gy. As seen in Figure 4.3 the surviving fractions for relative doses between 1.2 and 10 had surviving fractions of 65% or higher. It can be seen that for lower relative doses, i.e. below 6, the surviving

fraction did not follow the linear trend as well as for the higher relative doses. Typically, when irradiating cells, the more dose applied to the cells, the greater the cell death observed, which is demonstrated in our results [3]. However, our results deviated from the established literature in that the survival rates were much greater than anticipated. This experiment was re-designed from looking at the sensitization effects of Cerium Oxide NPs, and survival curves for this particular cell line. With those previous experiments an LD50 for the MCF7 cell line was found between 35-55 cGy [66, 67], while the LD50 that can be extrapolated from this current data set would be over 15. This large disparity implies the dose received is much lower than originally thought.

While gathering the initial survival curve (Figure 4.3), treatment with PEG-coated GNPs at the concentration of 34 nM was tested at the relative doses of 4, 5, and 6 (Figure 4.4). There is evidence from Figure 4.4 that the 34 nM indicated some potential to increase cell death. The relative dose of 4, showed the greatest difference in surviving fraction with a surviving fraction with no NPs survival observed to be 74% while the 34 nM concentration added dropped the surviving fraction to 63%. This difference produced an SER of about 1.2 $\pm$ 0.4. While the SER for the relative dose at 3 and 5 were 1.05 $\pm$ 0.05 and 1.1 $\pm$ 0.2 respectively indicating a small level of potential sensitization by being above 1. But still having uncharacteristically high surviving fractions prompting the use of TRIM to understand if the dosimetry was off. The TRIM simulation served as an additional way to determine where the beam energy was being deposited.

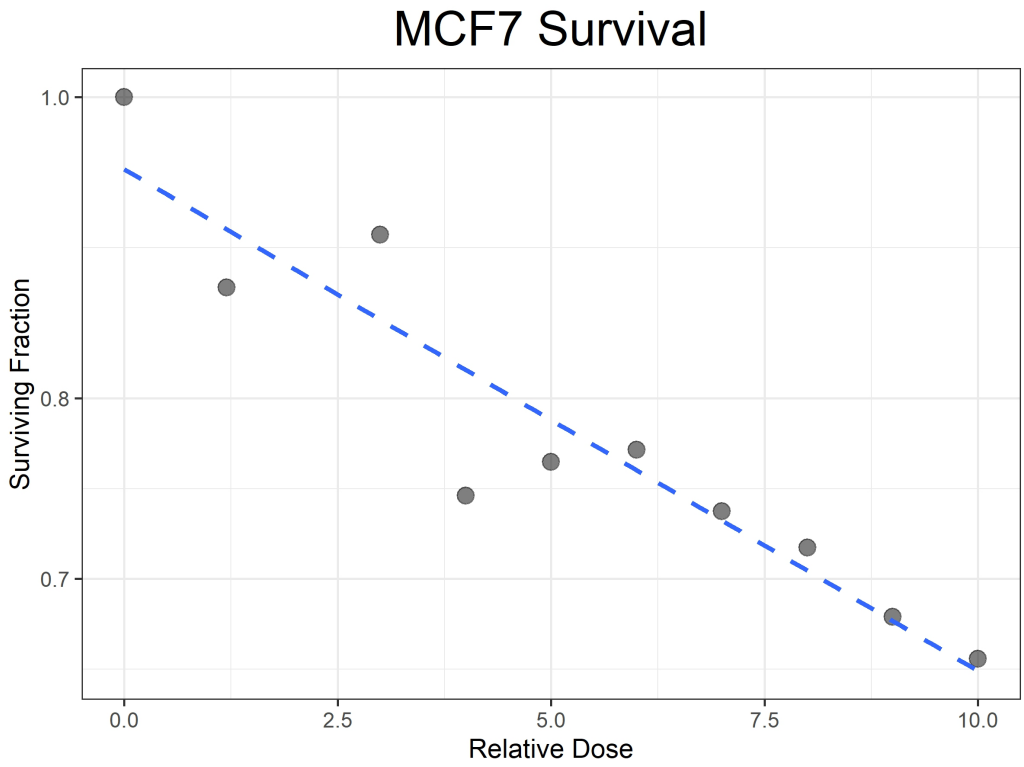

Figure 4.3: The scatter plot shows the survival curve for the MCF7 cell line on the custom 15-well plates for a range of relative doses from 1.2-10. The equation of the line of best fit was $y = -0.03x + 0.94$ which produced an R^2 value of 0.86.

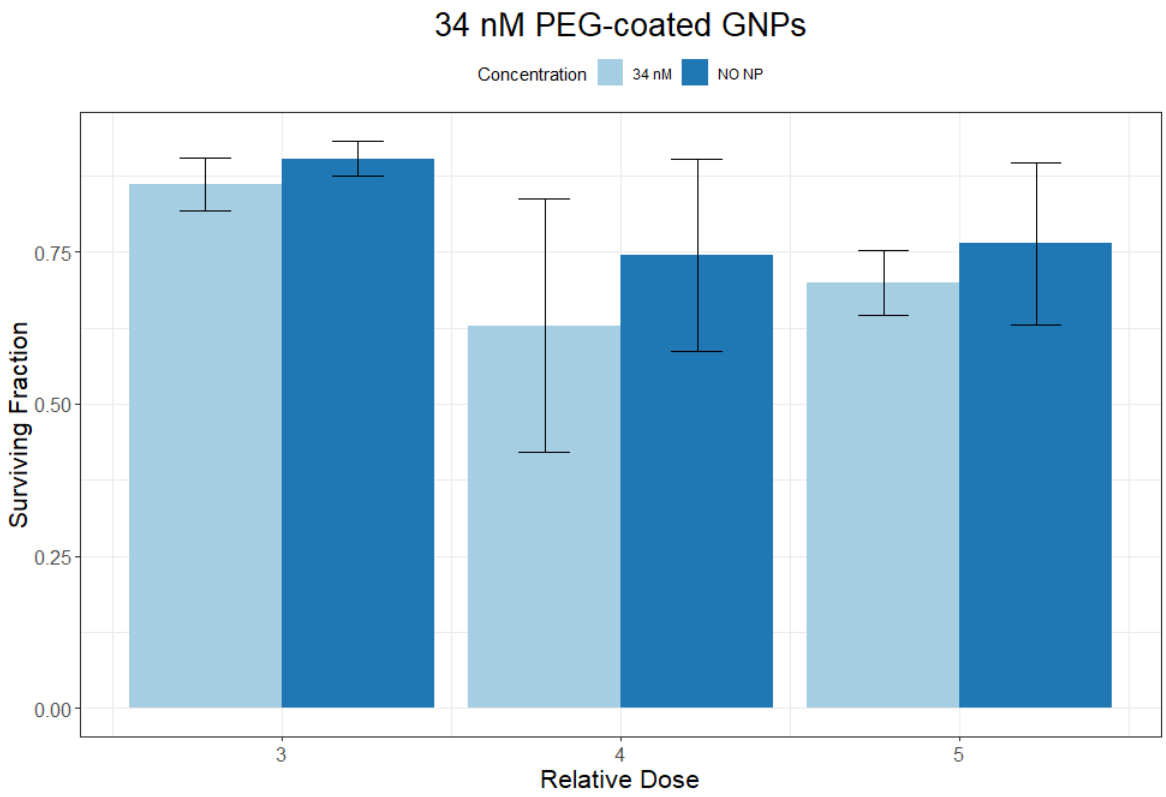

Figure 4.4: The bar plot showed the surviving fractions of No NP concentration (dark blue) to the 34 nM concentration (light blue) for relative doses 3, 4, and 5.

Figure 4.5 shows the particle trajectory made from the TRIM software [61]. It shows the particles path through the Havar exit window, followed by 24 mm of air and finally to the Mylar film which was the top and bottom of the custom wells. What is seen in Figure 4.5 and 4.6 is that some of the particles are losing energy in the Havar, which was expected, but the majority of the protons are stopping at the Mylar surface and depositing all their energy in the Mylar and not on the mono-layer of cells. Because the majority of the energy is lost to the Mylar film and not the mono-lay of cells, the survival potentially produced would be skewed higher than anticipated, which is what was seen in Figure 4.5 and 4.6.

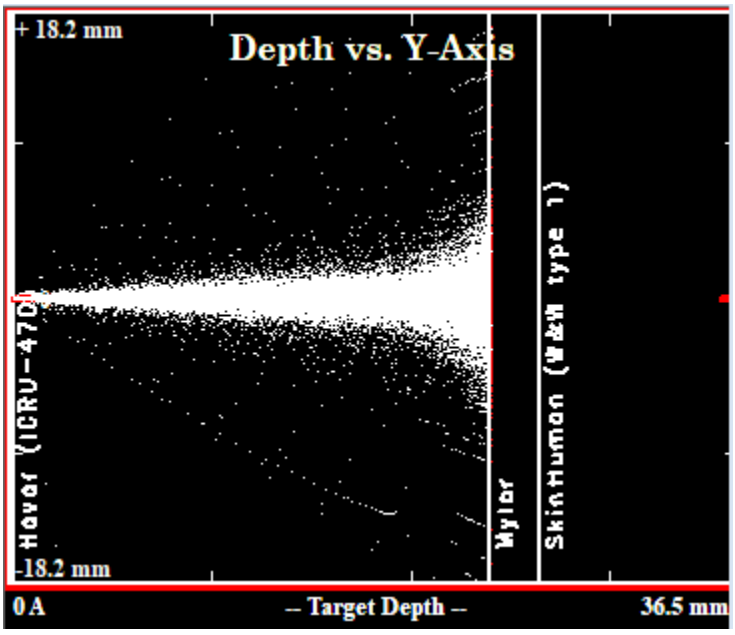

Figure 4.5: This figure was made through use of the TRIM simulation and shows the proton beams trajectory through the Havar exit window, through 24 mm of air and then through the Mylar on the Custom plates.

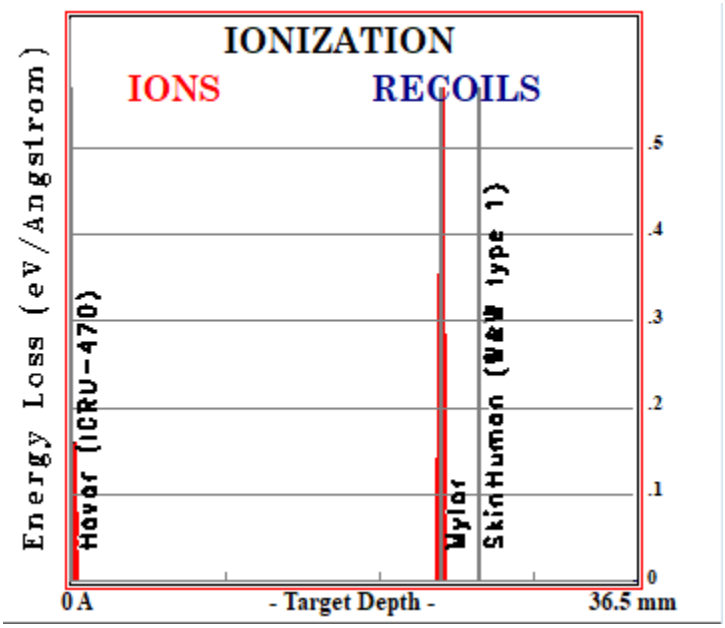

Figure 4.6: This figure shows the proton beam's energy loss through the Havar exit window, through 24 mm of air and then through the Mylar on the Custom plates. This graph was made based off of Figure 4.5 using the TRIM software.

Because of the inconsistent results to the previous iterations of experiment an experimen-

tal re-design was needed. For that reason TRIM was used to explore different variations of this experimental set-up to fine-tune the set-up.This was done by changing the experiment from the custom plates to an in air experiment with 96-well plates, as well as decreasing the distance the beam traveled in air. This was similar to the original design [66, 67].

4.3 96-Well Plate Survival Curve Results

The 96-well plate experiment was altered from the custom plate experiment to have more accurate deposition of dose on the MCF7 cell line. Figure 4.7 shows the TRIM simulation of the beam's trajectory through the Havar exit window, through 17 mm of air and finally to the mono-layer of cells. Compared to Figure 4.5, it is evident that the protons are no longer stopping short of the mono-layer of cells, and depositing the bulk of the energy as intended. Figure 4.8 also shows where the potential energy loss would happen along the beams trajectory. The first noticeable amount, was being lost to the Havar exit window. The rest of the energy loss is happening at the cell layer, implying placing the 96-well plates closer to the exit window, places the cells within the Bragg peak region of the proton beam; and maximized the potential dose deposition. Now that the simulation supported the new experimental set-up new survival curves were produced, and concentrations of 68 nM, 45nM, and 15 nM were tested for sensitization effects over a relative dose range between 2 and 11.

Figure 4.9 shows the scatter plot of the MCF7 cell line for relative doses ranging from 2 to 11. It can be seen that the surviving fraction is much lower than what was presented in Figure 4.3. Using the prestoBlue assay, the surviving fractions were constructed and from these curves the 50% survival can be determined from the fit line and compared as the treatment of NPs are added to the cell line. With this particular cell line the custom plate experiment produced 50% survival at a relative dose of 16.45, while Figure 4.9 shows 50% survival at a relative dose of 4.66. This while not as low as what was found with the previous iteration of the experiment [67, 66], is much more realistic than what was found in the custom plate experiments. And implies the changes done based off the TRIM simulations

enhanced the relative dose to the mono-layer of cells.

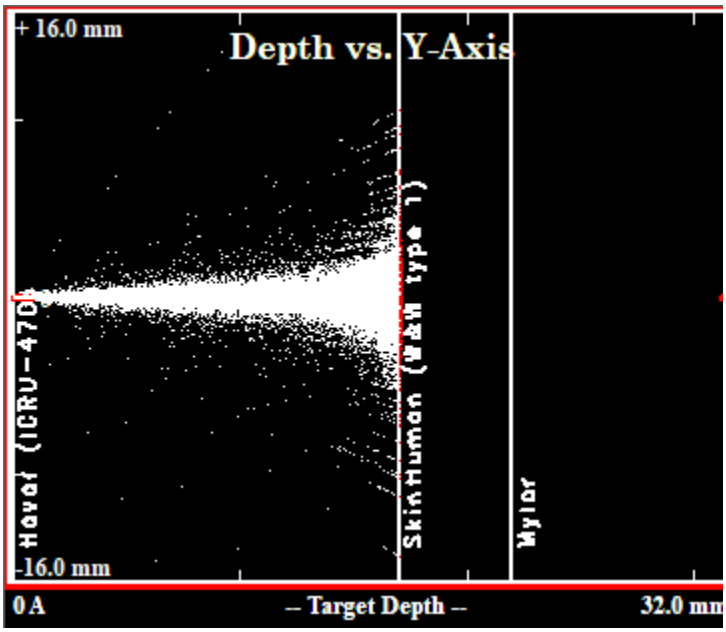

Figure 4.7: This figure shows the proton beams trajectory through the Havar exit window, through 17 mm of air and then to the cells. the ion beams trajectory seems to end right at the layer of cells.

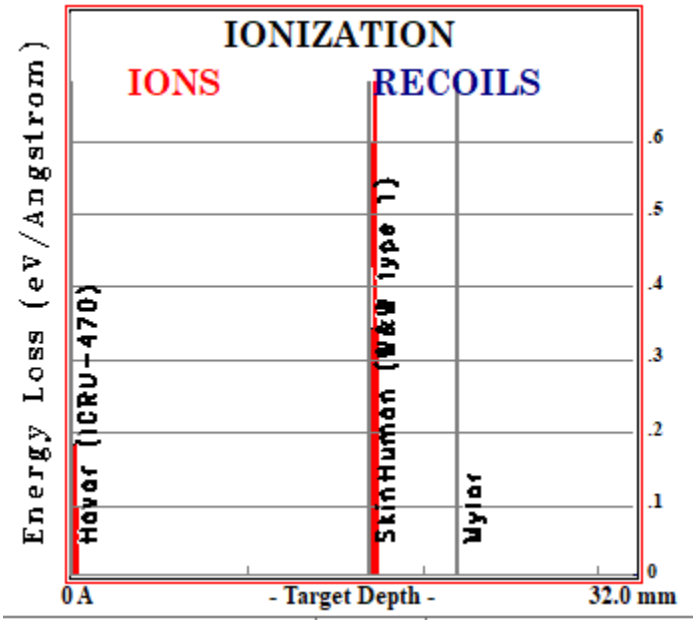

Figure 4.8: This figure shows where the energy loss is projected to happen for the 3 MeV proton beam. First loss is happening in the Havar exit window, which was expected based off the SRIM, the rest of the energy is seen to be lost in the cell layer.

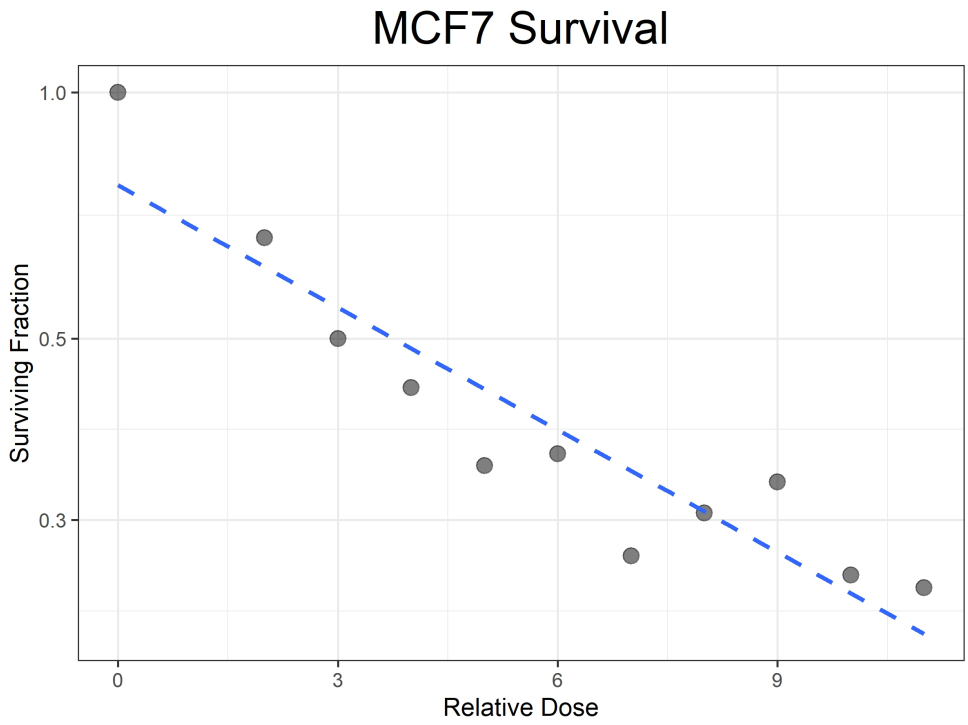

Figure 4.9: This scatter plot shows the surviving fraction of the MCF7 cell (45,000 cells per well) line when irradiated with a 3 MeV proton beam at varying exposure times. The red vertical line represents the LD50 line, which is resting at a relative dose of about 3.1.

4.4 96-Well Plate PEG-coated GNP Sensitization Results

Figure 4.10 shows how all three treated MCF7 cell survival curves compare with the non-treated MCF7 cell line (purple dashed line). The trend lines for the 3 concentrations at lower relative doses tended to yield a surviving fraction greater than the control data (No NPs). However at relative doses greater than about 4 the surviving fractions tended to be less than the control group. With the 15 nM concentration trend line tending to follow the closest to the control group. Figure 4.10 shows that as GNP-concentrations treatments increased they were observed to have a lower surviving fraction compared to the No NP treatment trend line, demonstrating a potential radiosensitization effect. With each of these trend lines the surviving fraction at 50% was extrapolated using the equation of the lines determined by the line of best fit presented. For the No NP trend line the equation was approximately $y = -0.056x + 0.761$. For the 15 nM trend line the equation was estimated

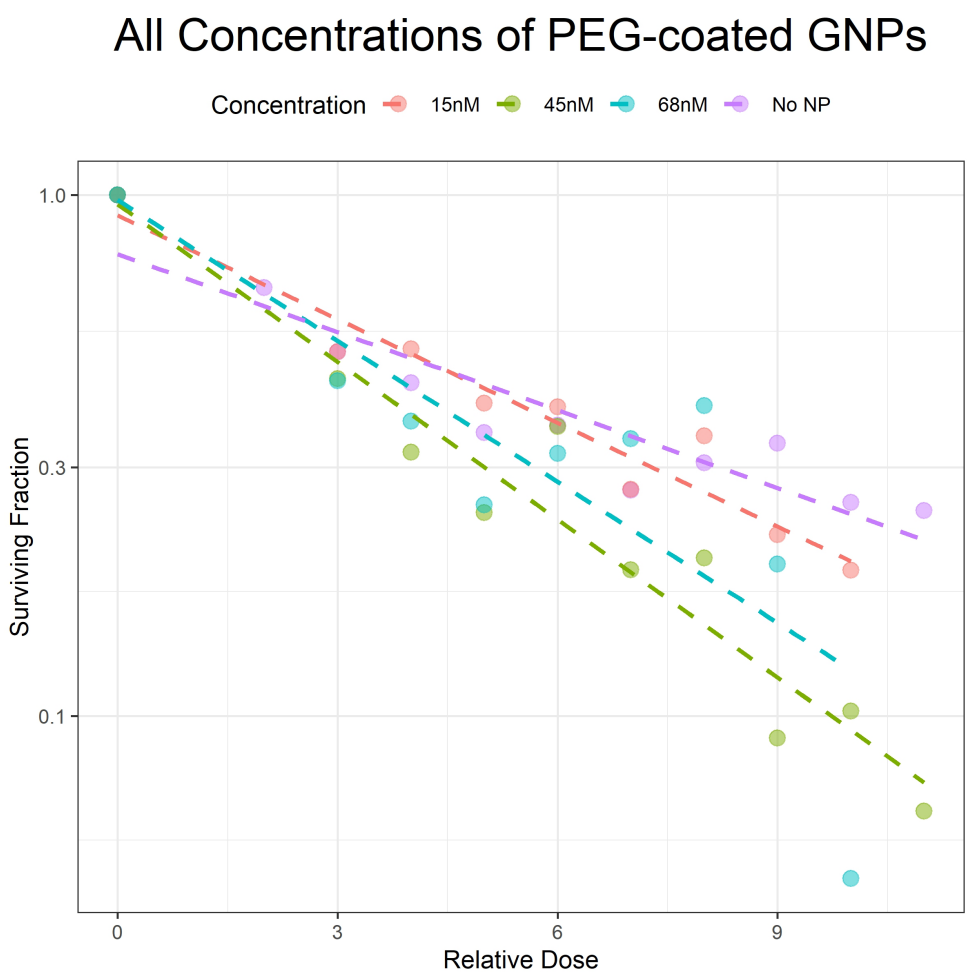

Figure 4.10: This scatter plot shows the surviving fraction of the MCF7 cell with all three concentrations (15, 45, and 68 nM) of PEG-coated GNPs when irradiated with a 3 MeV proton beam at varying relative doses. The R^2 values for the No NP, 15 nM, 45 nM, and 68 nM were 0.75, 0.86, 0.80, and 0.73 respectively.

to be $y = -0.071x + 0.837$. The 45 nM trend line was estimated to be $y = -0.072x + 0.757$, while the 68 nM trend line was estimated to be $y = -0.071 + 0.784$. As mentioned in the last section, the LD50 for the MCF7 No NP treatment wells was around a relative dose of 4.66. If the NP concentrations indicated sensitization the LD50 would potentially come in lower than the No-NP treated cells. From figure 4.10 the LD50 for the 15 nM concentration was slightly higher around 4.73 while the 45 nM and the 68 nM were extrapolated to be relative doses of 3.56 which translated into a 26.72 % difference in survival and 3.99 which translated into a 15.4% difference in survival respectively to the control data.

Figure 4.11 shows the direct comparison of the surviving fractions for the No NP wells compared to the 15 nM treated wells across the full range of relative doses, it is observed that at the relative doses of 9 and 10, are the only relative doses that indicated some kind of decrease in survival compared to the No-NP treated cells. The surviving fraction for relative dose 9 starts at about 33% (No NPs) and drops to 22% with the introduction of the 15 nM PEG-coated GNPs, which is a substantial drop. In table 4 the p-values are displayed, for this experiment statistical significance was marked at $p < 0.05$, at relative dose 9 the p-value is 0.0354, indicating statistical significance in the surviving fraction from from NO treated cell compared to treated cells. This particular relative dose also corresponded to SER value of 1.5±0.3 (table 4) which showed signs of decent sensitization with the SER >1. While similarly at relative dose 10 the surviving fraction starts at 26% and drops to about 19% yielding an SER of 1.3±0.2. While the drop in surviving fraction is not as substantial of a drop as at relative dose 9, it had a p-value equal to 0.0433, indicating statistical significance. This was not the case for any of the other relative doses, instead what seemed to happen was either an increase in survival or no change at all in survival. This increase can be seen reflected in Figure 4.11, at relative doses 4, 5, 6, and 8 where No-NP treated cells had a lower surviving fraction than the NP treated cells. At relative doses 3 and 7; there was no change in surviving fraction between the treated and No-NP treated cells surviving fractions around 50% at relative dose 3 and 27% at relative dose 7. The SER values (listed in table 4) were calculated to equal 1 for relative doses 3 and 7, and < 1 for the 4, 5, 6, and 8 relative dose treatments. The p-values for all relative doses except 9 and 10 reflected in table 4 show no statistical significance which matches the visualization of Figure 4.11.

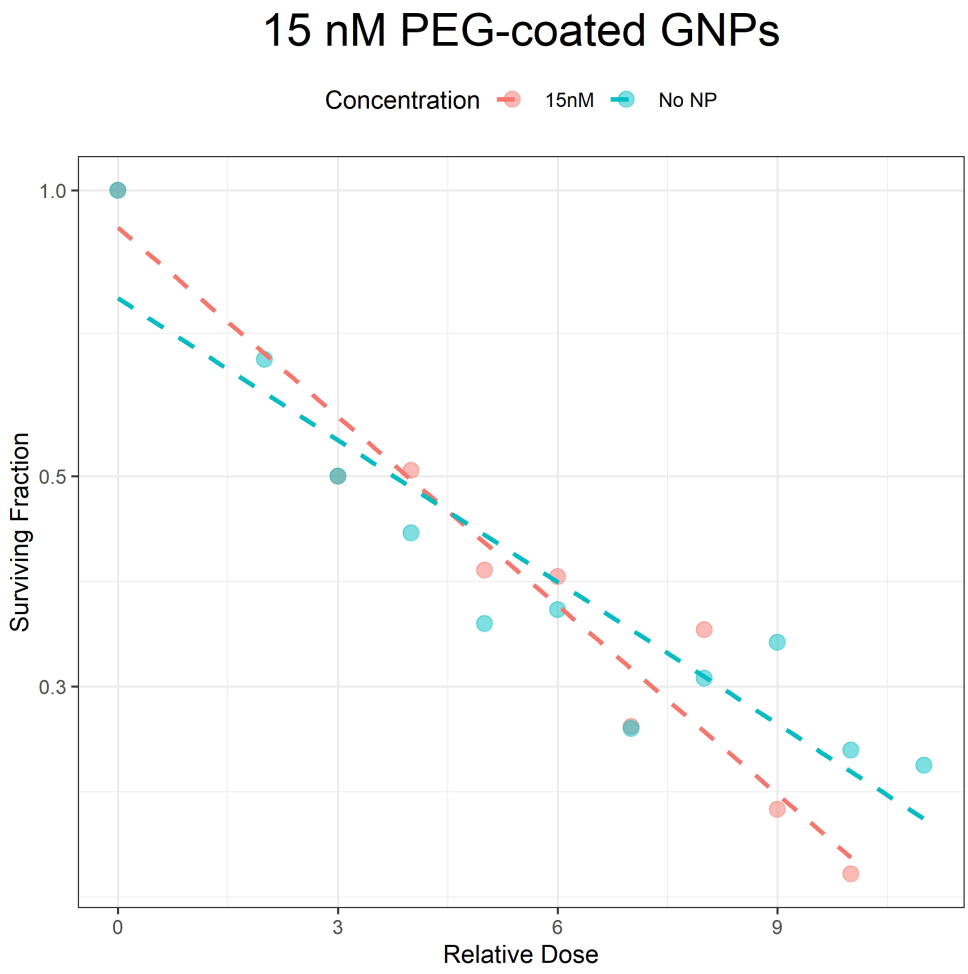

Figure 4.11: The scatter plot shows the difference in surviving fraction for the wells treated with 15 nM PEG-coated GNPs (pink dots) which yield an R^2 value of 0.86 against the wells not treated with any NPs (cyan dots) which yield an R^2 value of 0.75.

Relative Dose	3	4	5	6	7	8	9	10
p-value	0.9854	0.4707	0.6719	0.5632	0.3179	0.9489	0.0354	0.0433
SER±Uncertainty	1.0±0.1	0.9±0.1	0.9±0.1	0.9±0.1	1.0±0.2	0.9±0.3	1.5±0.3	1.3±0.2

Table 4: This table shows the determined p-values for the 15 nM concentration for PEG-coated GNPs, statistical significance is seen at $p < 0.05$. It also shows the SER ± uncertainty for each relative dose

Figure 4.12 compares cells treated with the 45 nM PEG-coated GNPs compared to the well that had no-NP treatment cells from relative doses 3 to 11. In Figure 4.12 it is observed that all the relative doses, expect for 6, the 45 nM treatments had lower surviving fractions than the untreated cells. The relative doses above 6 tended to have the largest difference

between survival fractions, where relative dose 7 showed the No-NP treated cell survival at 27% compared to the treated cells surviving fraction of 18%. This yielded an SER of 1.4±0.4 (table 5) and a p-value of 0.333 implying no statistical significance even though there was a substantial drop in percentage and SER > 1. At relative dose 8 the surviving fractions went from 31% to 19%, with an SER vale of also 1.4±0.4, with a p-value of 0.043 showing a statistically significant effect. The relative doses 9, 10 and 11 showed the largest decreases in survival in treated cells compared to No-NP treated cells,dropping from 33% to 9%, 26% to 10% and 25% to 6%, respectively. In table 5 their reflective p-values were calculated to be well below 0.05 implying a high level of statistical significance. These survival drops can also be seen at the lower dose ranges, where relative doses 3, 4, and 5 decreased from 50% to 44%, 44% to 32% and 35% to 24% respectively in the treated cells compared to the No-NP treated cells. All three of the lower end relative doses showed survival decreases compared to their No-treated counterpart, in table 5 relative doses 4, 5, 8, 9, 10, and 11 show statistically significance effects. The 45 nM treatment SER values in table 5, were all greater than 1, with the exception of relative dose 6 where the SER is equal to one. The highest SER values are observed at relative dose 11, where the SER is 3.8±1.8 and relative dose 9 observed to have an SER of 3.7±1.4. Relative dose 10 was also greater than 2 with an SER at 2.5±0.2 all implying potential sensitization effects for those relative doses and particular nM concentrations.

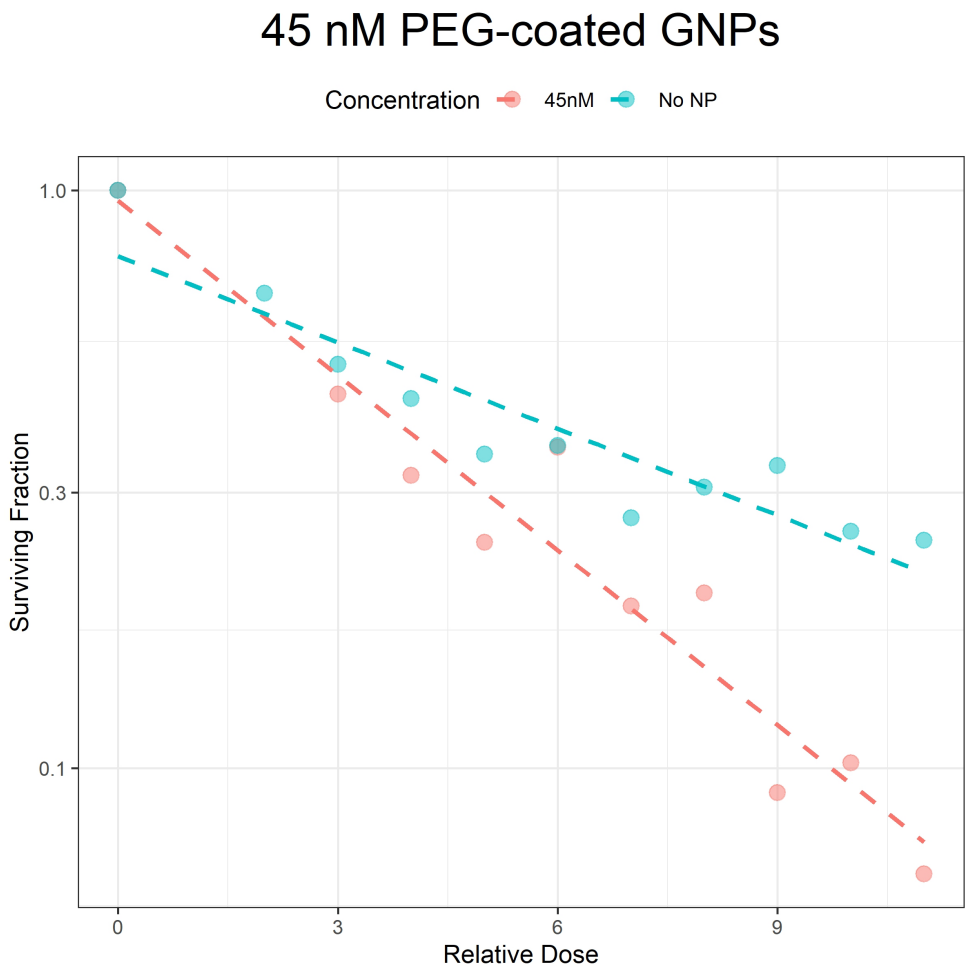

Figure 4.12: The scatter plot shows the difference in surviving fraction for the wells treated with 45 nM PEG-coated GNPs (pink dots) which yield an R^2 value of 0.80 against the wells not treated with any NPs (cyan dots) which yield an R^2 value of 0.75. The error bars represent the uncertainty within the calculated surviving fractions.

Relative Dose	p-value	SER±Uncertainty
3	0.305	1.3±0.2
4	0.015	1.4±0.2
5	0.023	1.4±0.3
6	0.580	1.0±0.2
7	0.333	1.4±0.4
8	0.043	1.4±0.4
9	1.62×10^{-7}	3.7±1.4
10	6.16×10^{-6}	2.5±0.2
11	9.32×10^{-5}	3.8±1.8

Table 5: This table shows the determined p-values for the 45 nM concentration for PEG-coated GNPs, statistical significance is seen at $p < 0.05$. The SER±Uncertainty is also listed for comparison.

The last concentration for the PEG-coated GNPs that was measured was 68 nM (Figure 4.13). The 68 nM concentration treatments showed sensitization effects at low relative doses (3-6) the surviving fraction observed for the treated cells compared to the No-NP treated wells. Drops in survival for relative doses 3, 4, 5, and 6 in treated compared to No-NP treated cells were 50% to 44%, 44% to 36%, 35% and 36% to 31%. A similar drop was seen in the the higher relative doses (9 and 10) going from 33% to 19% and 26% to 5%. Relative doses 7 and 8 had a surviving fraction that was observed to be larger for the cells treated with 68 nM of PEG-coated GNPS. The significance of these drops in survival are shown in Table 6, where the calculated p-values are displayed. Significant p-values were obtained for relative doses 5, and 9. The rest of the decreases in survival were not classified as significant ($p > 0.05$). The greatest difference in surviving fraction was observed at relative dose 10, yielding the highest SER value, 5.2± 4.1 (table 6). However with a p-value of 0.0844 this effect was not considered statistically significant. It is worth noting that the uncertainty for relative dose 10 for that particular SER value was very large in comparison to the calculated SER value which likely contributes to it not yielding a statistically significant difference. The SER values presented in table 6 for the 68 nM concentration did typically produce values > 1, with the exception of relative doses 7 and 8 with SER values of 0.8. The rest of the relative doses SER values ranged between 1.1 to 1.7.

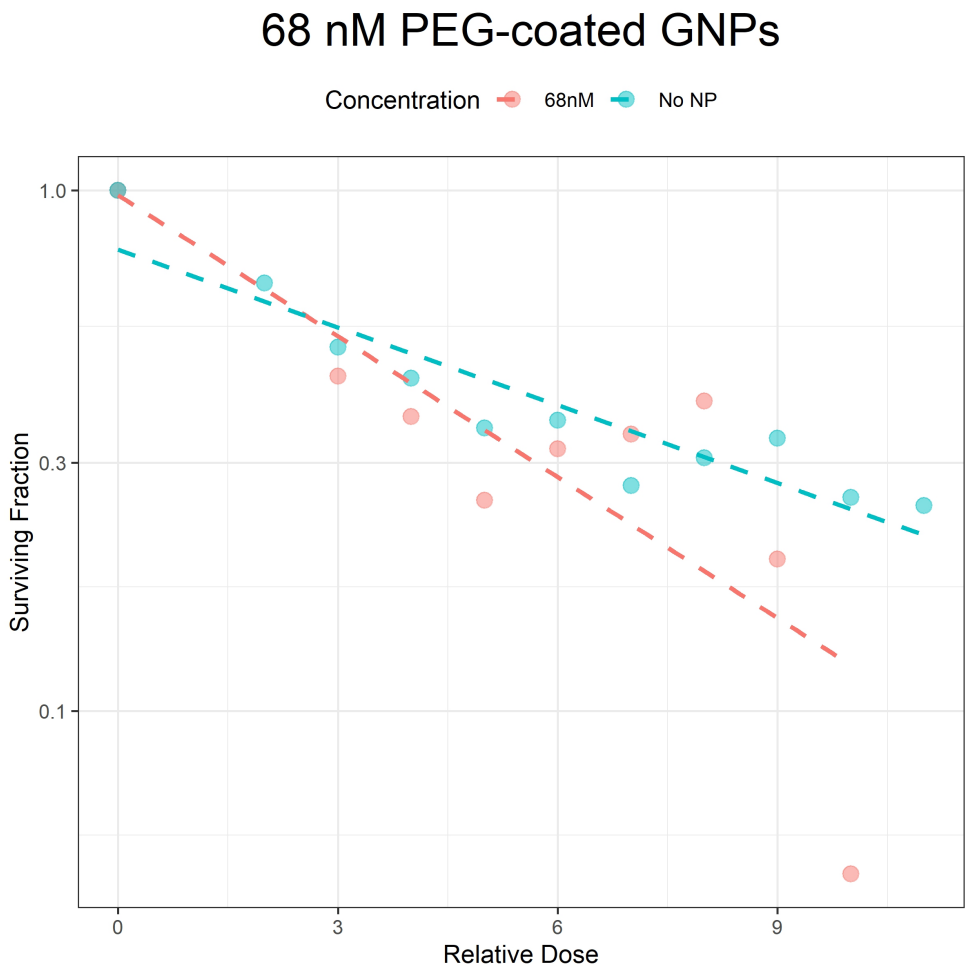

Figure 4.13: The scatter plot shows the difference in surviving fraction for the wells treated with 68 nM PEG-coated GNPs (pink dots) which yeild an R^2 value of 0.73, against the wells not treated with any NPs (cyan dots) which yield an R^2 value of 0.75. The error bars represent the uncertainty within the calculated surviving fractions.

Relative Dose	3	4	5	6	7	8	9	10
p-value	0.4506	0.1395	0.0453	0.2235	0.6247	0.4848	0.0070	0.0844
SER±Uncertainty	1.1±0.4	1.2±0.1	1.4±0.3	1.1±0.5	0.8±0.1	0.8±0.2	1.7±0.4	5.2±4.1

Table 6: This table shows the determined p-values for the 68 nM concentration for PEG-coated GNPs, statistical significance is seen at $p < 0.05$. The SER±Uncertainty is also listed for comparison.

45 nM and 68 nM GNP treatments both showed large decreases in the No-NP treated compared to treated surviving fractions, the 45 nM and 68 nM treatments were compared to examine if there were any meaningful differences between the two concentrations(Figure

4.14). The anticipation was that the 68 nM would yield a greater difference across the relative doses, but that was not the case. Only at relative doses 6 and 10 did the 68 nM concentration produce a lower surviving fraction than the 45 nM, with an observed difference of 32% to 36% and 5% to 10% respectively. At all other relative doses the surviving fraction was the same (3) or 45 nM was smaller (4, 5, 7, 8, and 9). Although only at relative doses 7, 8, and 9 was the difference large and the uncertainty bars did not over lap at all other relative doses there was overlap in the uncertainties. Further it is interesting to note the 68 nM concentration did not follow as dose dependent a trend as the 45 nM concentration did. That can be observed with the fist three relative doses (3, 4, and 5) steadily decreasing then, increasing to higher surviving fractions in the mid relative dose ranges (6, 7, and 8) and then dropping similar to the 45 nM concentration for the two highest relative doses.

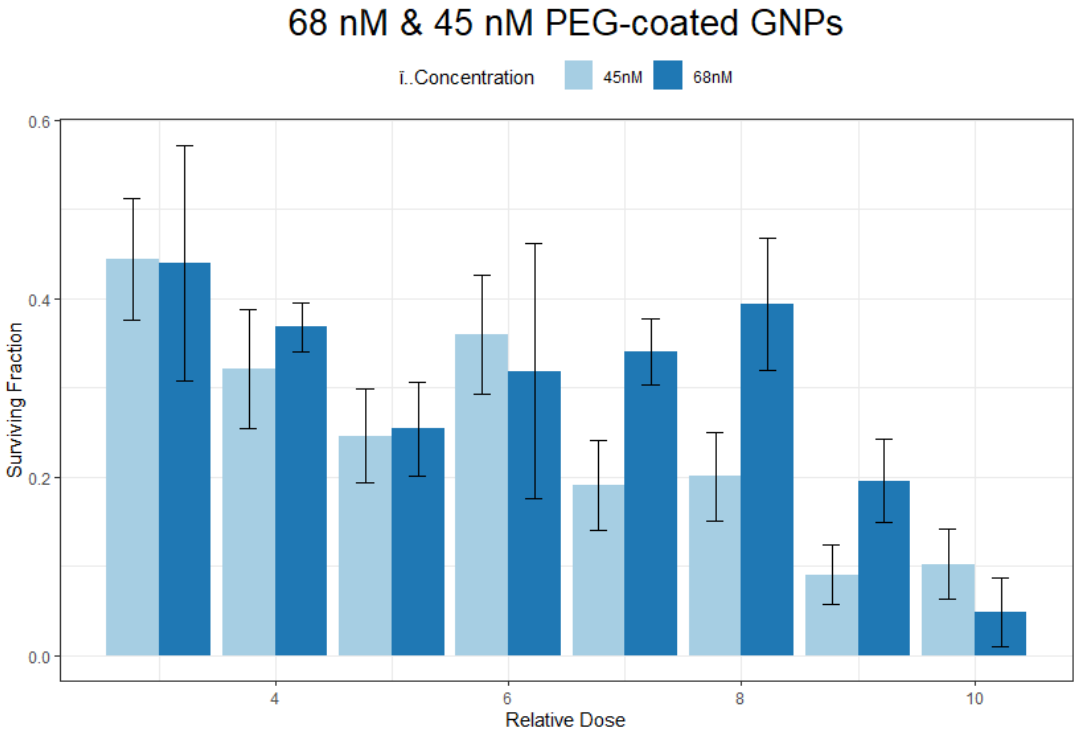

Figure 4.14: Comparative of the 45 nM (light blue bars) and the 68 nM (dark blue bars) concentration. The error bars represents the uncertainty for that given surviving fraction.

Relative Dose	3	4	5	6	7	8	9	10
p-value	0.9654	0.5646	0.8214	0.5529	0.05562	0.1549	0.06616	0.4359

Table 7: This table shows the determined p-values for the 45 nM compared to the 68 nM concentrations for PEG-coated GNPs, statistical significance is seen at $p < 0.05$.

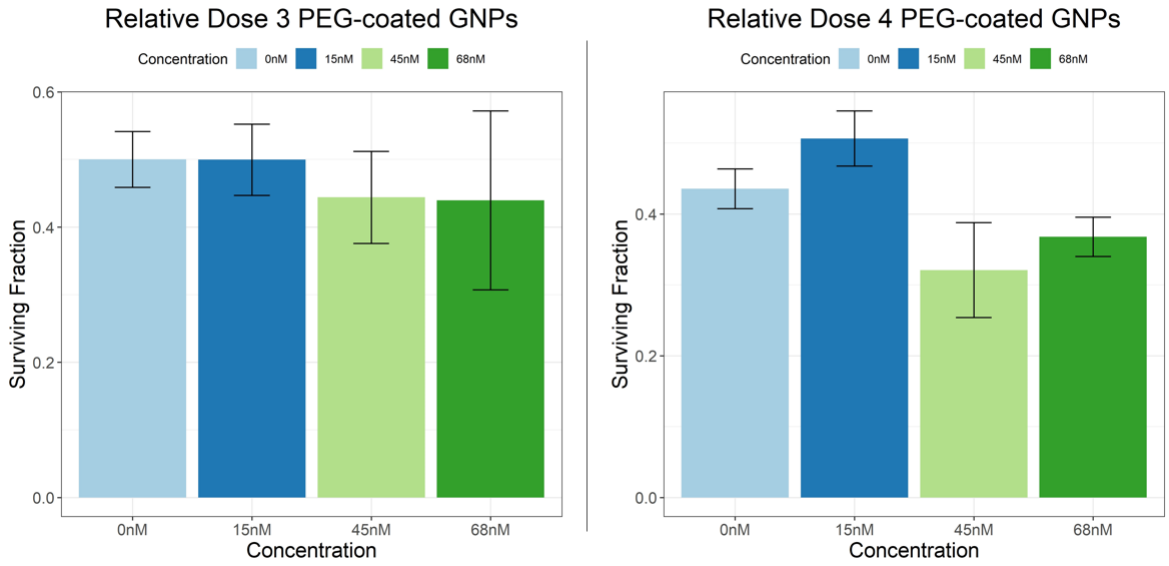

Figure 4.15: This figure shows the effects the concentrations may have on the surviving fractions for relative doses 3 and 4. The error bars represent the standard deviation of the sample pool for each concentration.

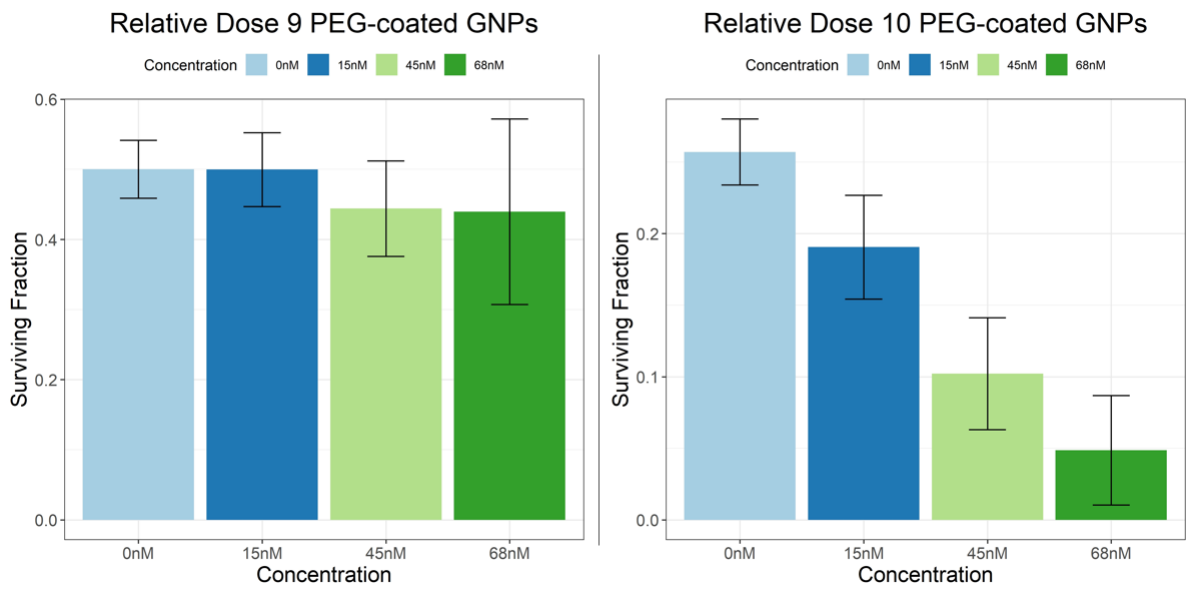

Figure 4.16: This figure shows the effects of the concentration may have on the surviving fraction for relative doses 9 and 10.

Figures 4.15 and 4.16 show the low and high dose results for the various concentrations compared to the controls. In Figure 4.15 low relative doses 3 and 4 are shown for no treatment as well as NP treatment of 15 nM, 45 nM, and 68 nM. For both the relative doses of 3 and 4 the concentration do not seem to have much influence on the surviving fraction. The uncertainty bars are made up of the standard deviation for each respective sample pool. The standard deviation of each sample was transformed into the standard error. Once standard error was obtained the surviving fractions and respective standard errors were used to calculate the uncertainty for each concentration. For the lower relative doses in Figure 4.15, it can be seen in tables 4, 5, and 6 there is no statistically significant difference in the surviving fractions. This implies at the lower dose range that the concentration did not influence the surviving fraction. However at the higher relative dose ranges, like shown in Figure 4.16 (relative doses 9 and 10), the concentration did seem to have some influence on the surviving fraction. It can be seen that typically the higher the concentration of PEG-coated GNPs the lower the surviving fraction. This can be seen particularly for relative dose 10 (Figure 4.16, right), where the higher the concentration the low lower the surviving fraction. The statistical

significance is also supported in tables 4, 5, and 6, where there was a p-value less than 0.05 for each concentration when compared to the control group. For relative dose 9 the results were a little less consistent as the surviving fraction at a concentration of 68 nM was higher than the surviving fraction at the 45 nM concentration, but all three concentrations yielded statistical significance compared to the control group (tables 4, 5, and 6).

4.5 96-Well Plate Sensitization Effects for PEG-coated SPIONs

For the PEG-coated SPIONs, concentrations of 136 nM, 45 nM, and 15 nM were experimentally tested through the 96-well plate in air configuration. Figure 4.17 shows the comparison of the No-NP treated cells to the 15 nM treated cells at relative doses of 3, 5, 7, and 9. A small drop in survival for relative doses 3 and 5 can be seen in the figure, with respective cell survival drops, 47% to 37% and 44% to 29% in No-NP treated and treated cells. The significance of the differences are displayed in table 8, and while relative doses 3 and 5 show a drop in survival their p-value are above the significance level. At the higher relative dose ranges, 7 and 9, opposite trends of increases in cell survival in treated cell were observed. The cells treated with 15 nM PEG-coated SPIONs had their survival fractions increase from 29% to 55% (7) and 31% to 37% (9). These changes at each relative dose are also depicted in table 8, with SER values. For relative dose 3 and 5 the SER values were > 1, (1.1 ± 0.1 and 1.3 ± 0.3), but as previously stated for the higher relative doses the surviving fractions increased with the introduction of the NPs yielding SER values < 1 for both 7 and 9 (0.5 ± 0.2 and 0.9 ± 0.2). The only relative dose that showed signs of a significant difference was the survival increase in survival at 7.

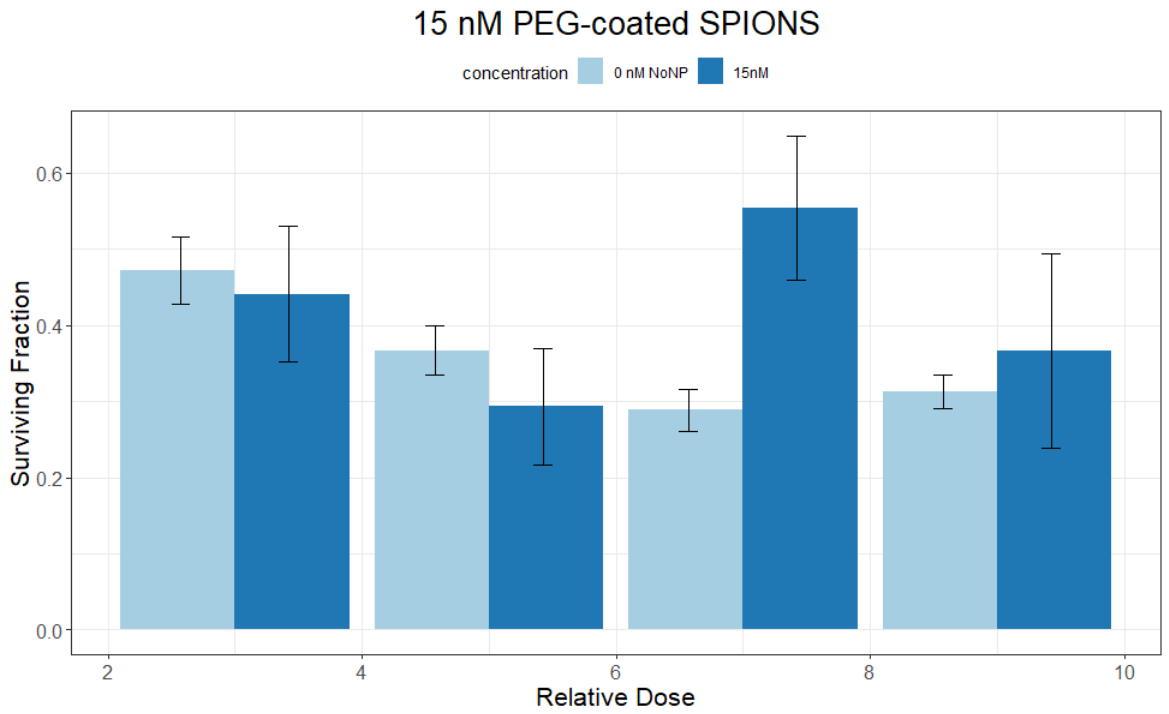

Figure 4.17: This bar graph represents the 15 nM PEG-coated SPIONs compared to the No-NP treated cell at relative doses 3, 5, 7, and 9. The error bars represent the uncertainty for the surviving fraction.

Relative Dose	3	5	7	9
p-value	0.5153	0.7561	$0.1.55\times10^{-5}$	0.4041
SER±Uncertainty	1.1±0.1	1.3±0.3	0.5±0.2	0.9±0.2

Table 8: This table shows the determined p-values for the 15 nM concentration for PEG-coated SPIONs, statistical significance is seen at $p < 0.05$. The SER±Uncertainty is also listed for comparison.

The results comparing 45 nM PEG-coated SPIONs treated cells to no-NP treated cells are shown in Figure 4.18. It can be observed that over most of the relative doses (3, 7, and 9) the surviving fraction of the treated cells were higher than the non-treated cells. The surviving fraction for the non-treated cells was anticipated to be higher than the treated cells, but that was only the case at relative dose 5. Because of the higher surviving fractions for the NP treated cells the SER values at relative doses 3, 7, and 9 were < 1 (table 9). In table 9 the calculated p-value for statistical significance are displayed. The only relative dose yielding any significance was 7 which indicated significance in the increase of survival,

not decrease.

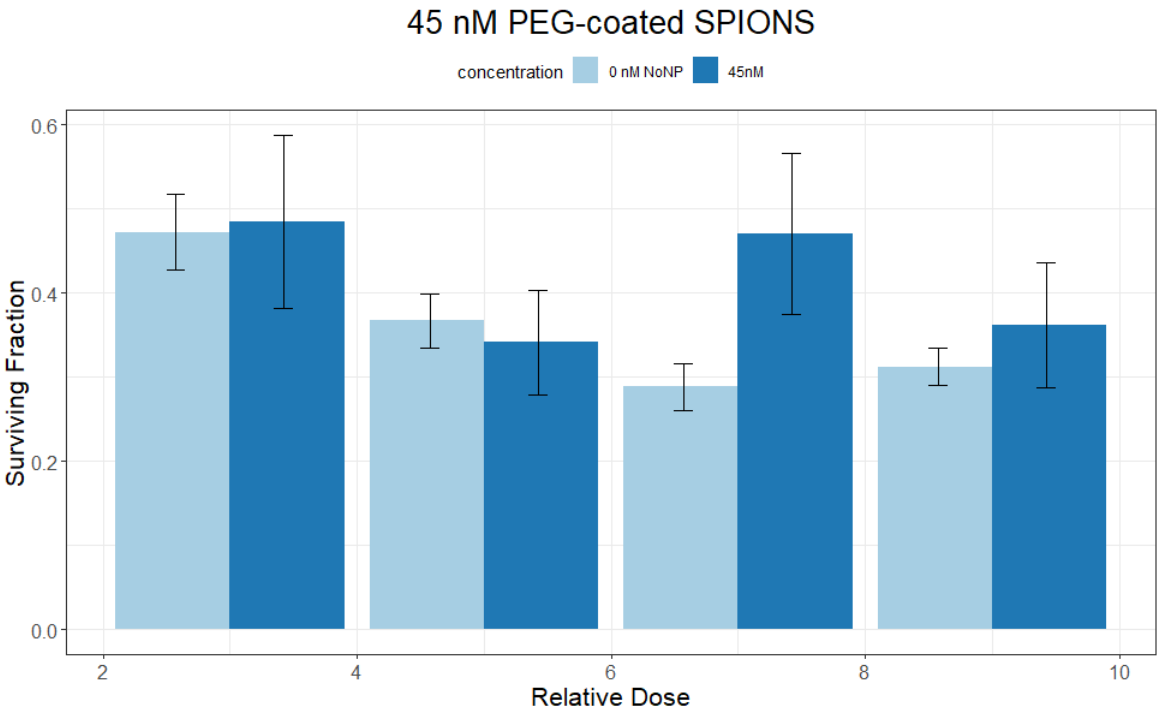

Figure 4.18: This bar graph represents the 45 nM PEG-coated SPIONs compared to the non-treated cell at relative doses 3, 5, 7, and 9. The error bars represent the uncertainty for the surviving fraction.

Relative Dose	3	5	7	9
p-value	0.4831	0.6027	0.0256	0.1603
SER±Uncertainty	1.0±0.1	1.1±0.4	0.6±0.3	0.9±0.1

Table 9: This table shows the determined p-values for the 45 nM concentration for PEG-coated SPIONs, statistical significance is seen at $p < 0.05$. The SER±Uncertainty is also listed for comparison

Figure 4.19 shows the difference between the No-NP treated cells compared to the 136 nM SPION NP treated cells. For each relative dose the surviving fractions are compared. With the surviving fraction at relative dose 3 for No-NP treated cells compared to the treated cells was 47% to 39%. At relative dose 5 the surviving fraction of No-NP treated cells compared to treated was 36% to 27%. For relative dose 7 an increase in the surviving fraction was 29% for non-treated cell and 36% for cells treated. At relative dose 9 the surviving fraction for No-NP treated cells compared to treated cells was 31% to 20%. These differences are

also reflected at SER values in table 10, where the SER value compares the two percentages and when > 1 implies sensitization is happening. For relative dose 3 the SER was 1.2 ± 0.2, for 5 it was 1.4 ± 0.1, for 7 it was 0.8 ± 0.4 and finally for 9 it was 1.5 ± 0.3. The 136 nM concentration can be seen as the concentration that yielded the highest SER values across the tested relative dose range, with only one relative dose below one, 7. Although the 136 nM SPION treatment trends appeared to decrease in survival fractions across all relative doses except 7, no associated p-values yielded statistically significant differences compared to No-NP treated cell (table 10).

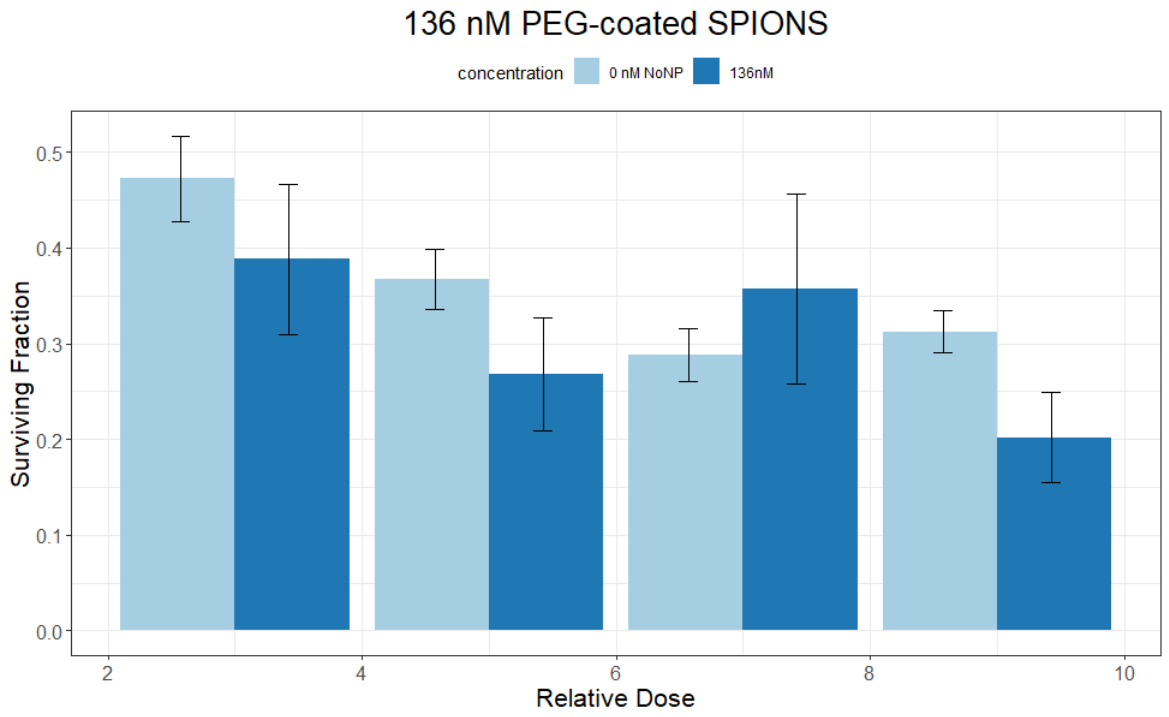

Figure 4.19: This bar graph represents the 136 nM PEG-coated SPIONs compared to the non treated cell at relative doses 3, 5, 7, and 9. The error bars represent the uncertainty for the surviving fraction.

Relative Dose	3	5	7	9
p-value	0.7505	0.2766	0.2812	0.2217
SER±Uncertainty	1.2±0.2	1.4±0.4	0.8±0.4	1.5±0.3

Table 10: This table shows the determined p-values for the 136 nM concentration for PEG-coated SPIONs, statistical significance is seen at $p < 0.05$. The SER±Uncertainty is also listed for comparison

5 Discussion

While the literature provides indication that high MeV proton beams (>40 MeV) when paired with GNPs have the potential to produce radio-sensitization [44, 20, 19, 18, 21]. The low proton energy range is still unclear. Some studies indicate enhancement in the SER and substantial decrease in surviving fractions with as little as 1.3 and 3 MeV [36, 45]. Others have observed with 3 MeV protons inconclusive results [42]. These inconsistencies are further reason why this study is important, to help enhance the understanding of low energy protons paired with metallic NPs.

5.1 PEG-coated GNP Discussion

With a realistic survival curve constructed based on the 3 MeV proton beam for the MCF7 cell line, a serial dilution was used to test 3 different PEG-coated GNP concentrations, 68 nM, 45 nM, and 15 nM. The prediction was: the greater the concentration of GNPs the greater the potential sensitization effects [39]. This did not exactly hold true for all of the concentrations. The 45 nM concentration yielded the best sensitization results across the board of relative doses, with the 68 nM having a slightly better sensitization effect at relative dose of 10, as seen in Figures 4.14 and 4.16 and tables 4, 5, and 6, which shows all of the SER results.

For sensitization effects it was important to not only look at the differences in surviving fractions and their calculated p-values but to also transform those surviving fractions into SER values. As previously discussed the sensitization enhancement ratio is a way to compare the surviving fraction of cells with a particular dose to that same dose but with a specific concentration of NPs. An SER value > 1 indicates that there was a positive sensitization effect happening at a particular dose with a specific concentration. The most dominate increased SER factors, shown in table 5, occurred with the 45 nM concentrations particularly at the higher relative dose ranges (9, 10, and 11) with each of these differences yielding a

p-value well below 0.05, indicating high statistical significance. There was an observed drop in surviving fraction that was apparent for each concentration (15 nM, 45 nM, and 68 nM).

The most inconsistent results for the PEG-coated GNPs came from the 15 nM concentration, with relative doses 9 and 10 being the only to yield an SER value > 1 (table 4). Only relative dose 9 was statistically significant with a p-value at 0.0354. The suspicion was for the MCF7 cell line the 15 nM concentration was too low to produce observable sensitization effects. There was a level of uncertainty if there was a significant amount of NPs that integrated into the cells. In fact, the 15 nM concentration was the only concentration for the PEG-coated GNPs that had an increased LD50 from the original cell line which was 4.66. The 15 nM concentration produced an LD50 at a relative dose of about 4.73. There was an observed percent increase of 1.53%, further solidifying that the 15 nM concentration for this particular cell line was inconsistent and would need further testing that confirmed a meaningful cellular uptake of GNPs. There is also the possibility of error occurring experimentally. For this experiment the low doses were hard to achieve, the exposure times to anything less than a relative dose of 5 were calculated to be around 2.5-3.5 seconds. Because these exposure times are so low, the likelihood of an incomplete exposure is possible. While the exposure time is monitored in a consistent manner between experiments, the beam stability is not always the same. With the low doses having such fast exposure times, that could yield inconsistent results and could possibly be why the trends do not fall as linearly as the higher doses do.

The results for the 68 nM concentration, while not completely consistent, but did yield more meaningful sensitization effects than the 15 nM concentration.The largest decrease in surviving fractions for the 68 nM cells came from relative doses 5 and 9. There was a noticeable drop in surviving fractions for both going from 35% to 25% and 33% to 20% respectively. These decreases gave p-values of 0.0453 and 0.007, where the relative dose of 5 shows statistical significance and the relative dose 9 shows high significance, implying if concentrations of 68 nM were to be further studied dose ranges between 5 and 9 would likely

yield a high level of sensitization. Especially with the SER value for 9 was calculated to be 3.7±1.4, one of the largest SER values of this experiment.

As for the 45 nM concentration it would be worth noting the decrease in LD50 and the surviving fractions across the relative dose ranges provided the most promise; the LD50 was observed to have a 26.72 % decrease, as opposed to the observed LD50 for 68 nM, observed to have a 15.4 % decrease from the LD50 for the No-NP treated cells. There were consistently lower surviving fractions across the relative dose range with the exception of relative dose 6, where there was no indication of drop in surviving fraction. However, the significant drops in surviving fraction was most statistically significant at relative doses 9, 10 and 11. There was statistical significance seen at dose 4, 5, and 8 as well, but not as prevalent at the higher relative doses. This overall decrease across the relative doses implies that for the MCF7 cell line paired with proton irradiation the 45 nM concentration may provide most optimal effects. When comparing the sensitization effects seen at the 45 nM and 68 nM concentration greater drop in surviving fraction happened more often with the 45 nM concentrations especially at relative doses 7, 8, and 9. While none of the differences yield a p-value less than 0.05 at relative doses 7 and 9 get close being 0.06 and 0.07 respectively. These results demonstrated that 45 nM GNP treatments yielded better sensitization effects compared to 68 nM, but more work is required to definitively make that claim. These results reflect 3 different experiments, and if more were to be performed it is likely the statistical significance could be more evident between which concentration would be more optimal.

When experimenting with biological material there are manypossible sources of error and inconsistencies that needed to be accounted for. With the culturing of cells, contamination can always happen. For this experiment great care was taken to account for cell death outside of irradiation, having several control plates that move through the environmental changes that the irradiated plates do. Because the cells are open to air, there were some wells that obtained contamination. The wells were monitored via a microscope to monitor morphology of the cells during each stage of the experiment. Their media color was also

monitor and if changes were apparent the wells would be marked for further evaluation, if contamination was evident the well would be pulled from the sample.

5.2 PEG-coated SPIONs Discussion

The PEG-coated SPIONs were compared at relative doses 3, 5, 7, and 9 for concentrations of 136 nM, 45 nM and 15 nM, the results were mostly inconclusive. These data sets were graphically and numerically analyzed for each concentration and while lower relative doses 3 and 5 typically showing a decrease in surviving fraction, none of it was statistically significant. The only statistical significance that was observed happened at relative dose 7 for the 15 and 45 nM concentrations, with increases in survival, rather than predicted decreases in survival. This overall increase in surviving fractions with PEG-coated SPION treatment implies the potential for radio protector rather than enhancer. More work is required to definitively state this, but it is an interesting potential effect of SPIONs. The SPION data was run over the course of 3 experiments, it would be worthwhile to run this experiment a couple times at this relative dose range to see if results can be consistently replicated, especially with the 15 nM and 136 nM concentrations as those two did yield some decrease in surviving fraction, even though it was not statistically significant.

The lab has a non-cancerous breast cell line, that could be a prime candidate to test the potential protector effects PEG-coated SPIONs may have.

5.3 Future Directions

The enhancements brought to this experiment was just the starting point. For further studies, it would be interesting to use the non-malignant breast cell line paired with the SPIONs and assess their potential as radio protectors. With the increased survival seen with the MCF7 line, it would be worthwhile to see if similar observations can be made with the non-malignant cells. Another starting place to mitigate the potential of cell death because of the exposure to air, the construction of a custom plate could be revisited. The Mylar for the

custom plate can be thinner, but more notably the exit window material can be revisited to find a metal that the beam would lose less energy to. The current Havar exit window is 10μm thick, and Havar foil as thin as 2.5 μm can be commercially purchased for experimental use. With the help of the TRIM simulations different material can be explored.

While the PEG-coated GNPs showed greater cell death implying dose enhancement, it would be a good next step to incorporate an additional metric for cell NP uptake. Based on the literature it is known the PEG-coating and size make the NPs prime candidates to be up-taken into the cells[38, 39, 35], but it would be great to visually see where and better characterize projected concentrations of how many NPs are uptaken into the cell [36]. Along with locating and counting how many NPs make it into the cells, it would be interesting to learn how to run a biological assay on analyzing the DNA damage that is ensuing from the protons and the consequent secondary interactions from the protons interacting with NPs. That would present a more conclusive mechanism to understand how and why cell damage is actually taking place.

The final future direction that is already in place is fine-tuned dosimetric analysis. With as low of a proton energy as this experiment has, it is difficult to confirm the dosimetry that has been projected based off of SRIM. In an attempt to find the Bragg peak for the proton beam, it was found that without use of Gafchromic film there cannot be a real dose confirmation. With the SRIM and TRIM analysis we have a decent projection of the dosimetry but it is not verified experimentally, which may be possible by exploring non-symmetric EBT2 film.

References

[1] Simon R. Cherry, James A. Sorenson, and Michael E. Phelps. *Physics in nuclear medicine*. 4th ed. London: Elsevier, 2012.

[2] Faiz M. Khan and Jr Gibbons John P. *Khan's the physics of radiation therapy*. 5th ed. Philadelphia: Lippincott Williams & Wilkins/Wolters Kluwer, 2014.

[3] Eric J. Hall and Amato J. Giaccia. *Radiobiology for the radiologist*. 7th ed. Philadelphia: Wolters Kluwer Health/Lippincott Williams & Wilkins, 2012.

[4] Frank H. Attix. *Introduction to radiological physics and radiation dosimetry*. 1st ed. New York: Wiley-VCH, 2004.

[5] Radhe Mohan. "A review of proton therapy – Current status and future directions". In: *Precision Radiation Oncology* 6 (2022), pp. 164–176.

[6] G. G. Steel, T. J. Mcmillan, and J. H. Peacock. "The radiobiology of human cells and tissues. In vitro radiosensitivity. The picture has changed in the 1980s". In: *International Journal of Radiation Biology* 56.5 (1989), pp. 525–537.

[7] W. S. Kendal. "The application of probability-generating functions to linear-quadratic radiation survival curves". In: *International Journal of Radiation Biology* 76.4 (2000), pp. 581–587.

[8] J. E. Turner. *Atoms, radiation, and radiation protection*. 3rd ed. Weinheim: Wiley-VCH, 2007.

[9] Hasan Murshed. *Fundamentals of radiation oncology: physical, biological, and clinical aspects*. 3rd ed. London;San Diego, CA; Academic Press is an imprint of Elsevier, 2019.

[10] R. R. Wilson. "Radiological use of fast protons". In: *Radiology* 47.5 (1946), pp. 487–491.

[11] Sandrine Lacombe, Erika Porcel, and Emanuele Scifoni. "Particle therapy and nanomedicine: state of art and research perspectives". In: *Cancer Nanotechnology* 8.1 (2017), pp. 9–17.

[12] Yao Chen, Juan Yang, Shaozhi Fu, and Jingbo Wu. "Gold nanoparticles as radiosensitizers in cancer radiotherapy". In: *International Journal of Nanomedicine* 15 (2020), pp. 9407–9430.

[13] B. Jeremic, A. R. Aguerri, and N. Filipovic. "Radiosensitization by gold nanoparticles". In: *Clinical and Translational Oncology* 15 (2013), pp. 593–601.

[14] MSc Rahman Wan N., PhD Bishara Nour, MSc Ackerly Trevor, PhD He Cheng F., BSc Jackson Price, BSc Wong Christopher, PhD Davidson Robert, and PhD Geso Moshi. "Enhancement of radiation effects by gold nanoparticles for superficial radiation therapy". In: *Nanomedicine* 5.2 (2009), pp. 136–142.

[15] D. B. Chithrani, S. Jelveh, F. Jalali, M. van Prooijen, C. Allen, R. G. Bristow, R. P. Hill, and David A. Jaffray. "Gold Nanoparticles as Radiation Sensitizers in Cancer Therapy". In: *Radiation Research* 173.6 (2010), pp. 719–728.

[16] James F. Hainfeld, Candice J. Foley, Suresh C. Srivastava, Leonard F. Mausner, N. I. Feng, George E. Meinken, and Zenon Steplewski. "Radioactive gold cluster immunoconjugates: Potential agents for cancer therapy". In: *International Journal of Radiation Applications and Instrumentation. Part B, Nuclear Medicine and Biology* 17.3 (1990), pp. 287,291–289,294.

[17] Mihaela Ghita, Stephen J. McMahon, Laura E. Taggart, Karl T. Butterworth, Giuseppe Schettino, and Kevin M. Prise. "A mechanistic study of gold nanoparticle radiosensitisation using targeted microbeam irradiation". In: *Scientific Reports* 7.1 (2017), p. 44752.

[18] Jerimy C. Polf, Lawrence F. Bronk, Wouter H. P. Driessen, Wadih Arap, Renata Pasqualini, and Michael Gillin. "Enhanced relative biological effectiveness of proton radiotherapy in tumor cells with internalized gold nanoparticles". In: *Applied Physics Letters* 98.19 (2011), p. 193702.

[19] Jong-Ki Kim, Seung-Jun Seo, Ki-Hong Kim, Tae-Jeong Kim, Myung-Hwan Chung, Kye-Ryung Kim, and Tae-Keun Yang. "Therapeutic application of metallic nanoparticles combined with particle-induced x-ray emission effect". In: *Nanotechnology* 21.42 (2010), p. 425102.

[20] Jong-Ki Kim, Seung-Jun Seo, Hong-Tae Kim, Ki-Hong Kim, Myung-Hwan Chung, Kye-Ryung Kim, and Sung-Jun Ye. "Enhanced proton treatment in mouse tumors through proton irradiated nanoradiator effects on metallic nanoparticles". In: *Physics in Medicine & Biology* 57.24 (2012), pp. 8309–8323.

[21] Dylan Peukert, Ivan Kempson, Michael Douglass, and Eva Bezak. "Metallic nanoparticle radiosensitisation of ion radiotherapy: A review". In: *Physica Medica* 47 (2018), pp. 121–128.

[22] James F. Hainfeld, Daniel N. Slatkin, and Henry M. Smilowitz. "The use of gold nanoparticles to enhance radiotherapy in mice". In: *Physics in Medicine & Biology* 49.18 (2004), N309–N315.

[23] James F. Hainfeld, F. A. Dilmanian, Daniel N. Slatkin, and Henry M. Smilowitz. "Radiotherapy enhancement with gold nanoparticles". In: *Journal of Pharmacy and Pharmacology* 60.8 (2008), pp. 977–985.

[24] James F. Hainfeld, F. A. Dilmanian, Zhong Zhong, Daniel N. Slatkin, John A. Kalef-Ezra, Henry M. Smilowitz, and Brookhaven National Laboratory (BNL). "Gold nanoparticles enhance the radiation therapy of a murine squamous cell carcinoma". In: *Physics in Medicine & Biology* 55.11 (2010), pp. 3045–3059.

[25] Tao Kong, Jie Zeng, Xiaoping Wang, Xiaoyan Yang, Jing Yang, Steve McQuarrie, Alexander McEwan, Wilson Roa, Jie Chen, and James Z. Xing. "Enhancement of radiation cytotoxicity in breast-cancer Cells by localized attachment of gold nanoparticles". In: *Small (Weinheim an der Bergstrasse, Germany)* 4.9 (2008), pp. 1537–1543.

[26] Xiaojing Zhang, James Z. Xing, Jie Chen, Lawrence Ko, John Amanie, Sunil Gulavita, Nadeem Pervez, Don Yee, Ronald Moore, and Wilson Roa. "Enhanced radiation sensitivity in prostate cancer by gold-nanoparticles". In: *Clinical and Investigative Medicine* 31.3 (2008), E160–E167.

[27] Sophie Grellet, Konstantina Tzelepi, Meike Roskamp, Phil Williams, Aquila Sharif, Richard Slade-Carter, Peter Goldie, Nicky Whilde, Malgorzata A. Smialek, Nigel J. Mason, and Jon P. Golding. "Cancer-selective, single agent chemoradiosensitising gold nanoparticles". In: *PloS One* 12.7 (2017), e0181103.

[28] B. Koger and C. Kirkby. "Dosimetric effects of polyethylene glycol surface coatings on gold nanoparticle radiosensitization". In: *Physics in Medicine and Biology* 62 (2017), pp. 8455–8469.

[29] Xiao-Dong Zhang, D. Wu, Xiu Shen, Pei-Xun Liu, N. Yang, Bin Zhao, Hao Zhang, Yuan-Ming Sun, Liang-An Zhang, and Fei-Yue Fan. "Size-dependent in vivo toxicity of PEG-coated gold nanoparticles". In: *International Journal of Nanomedicine* 6 (2011), pp. 2071–2081.

[30] Kyle Bromma and D. B. Chithrani. "Advances in gold nanoparticle-based combined cancer therapy". In: *Nanomaterials (Basel, Switzerland)* 10.9 (2020), pp. 1–25.

[31] Frank Alexis, Eric Pridgen, Linda K. Molnar, and Omid C. Farokhzad. "Factors affecting the clearance and biodistribution of polymeric nanoparticles". In: *Molecular Pharmaceutics* 5 (2008), pp. 505–515.

[32] Krzysztof Sztandera, Michał Gorzkiewicz, and Barbara Klajnert-Maculewicz. "Gold nanoparticles in cancer treatment". In: *Molecular Pharmaceutics* 16 (2019), pp. 1–23.

[33] Guodong Zhang, Zhi Yang, Wei Lu, Rui Zhang, Qian Huang, Mei Tian, Li Li, Dong Liang, and Chun Li. "Influence of anchoring ligands and particle size on the colloidal stability and in vivo biodistribution of polyethylene glycol-coated gold nanoparticles in tumor-xenografted mice". In: *Biomaterials* 30.10 (2008;2009;), pp. 1928–1936.

[34] Sushma Kommareddy and Mansoor Amiji. "Biodistribution and Pharmacokinetic Analysis of Long-Circulating Thiolated Gelatin Nanoparticles Following Systemic Administration in Breast Cancer-Bearing Mice". In: *Pharmaceutical Cciences* 96.2 (2007), pp. 397–407.

[35] Sameer Varma, Smita Dey, and Dhanabal Palanisamy. "Cellular uptake pathways of nanoparticles: Process of endocytosis and factors affecting their fate". In: *Current Pharmaceutical Biotechnology* 23 (2021), pp. 679–706.

[36] Sha Li, Sébastien Penninckx, Linda Karmani, Anne-Catherine Heuskin, Kassandra Watillon, Riccardo Marega, Jerome Zola, Valentina Corvaglia, Geraldine Genard, Bernard Gallez, Olivier Feron, Philippe Martinive, Davide Bonifazi, Carine Michiels, and Stéphane Lucas. "LET-dependent radiosensitization effects of gold nanoparticles for proton irradiation". In: *Nanotechnology* 27.45 (2016), p. 455101.

[37] Wilson Roa, Xiaojing Zhang, Linghong Guo, Andrew Shaw, Xiuying Hu, Yeping Xiong, Sunil Gulavita, Samir Patel, Xuejun Sun, Jie Chen, Ronald Moore, and James Z. Xing. "Gold nanoparticle sensitize radiotherapy of prostate cancer cells by regulation of the cell cycle". In: *Nanotechnology* 20.37 (2009), p. 375101.

[38] Xiaojing Zhang, James Z Xing, Jie Chen, Lawrence Ko, John Amanie, Sunil Gulavita, Nadeem Pervez, Don Yee, Ronald Moore, and Wilson Roa. "Enhanced radiation sensitivity in prostate cancer by gold-nanoparticles". In: *Clin Invest Med* • 31 (2008).

[39] B. D. Chithrani, Arezou A. Ghazani, and Warren C. W. Chan. "Determining the Size and Shape Dependence of Gold Nanoparticle Uptake into Mammalian Cells". In: *Nano Letters* 6.4 (2006), pp. 662–668.

[40] Daniel Y. Joh, Lova Sun, Melissa Stangl, Ajlan Al Zaki, Surya Murty, Phillip P. Santoiemma, James J. Davis, Brian C. Baumann, Michelle Alonso-Basanta, Dongha Bhang, Gary D. Kao, Andrew Tsourkas, and Jay F. Dorsey. "Selective targeting of brain tumors with gold nanoparticle-induced radiosensitization". In: *PloS One* 8.4 (2013), e62425.

[41] Lorenzo Torrisi. "Recent patents gold nanoparticles enhancing protontherapy efficiency". In: *Nanotechnology* (2015).

[42] J. C.G. Jeynes, M. J. Merchant, A. Spindler, A. C. Wera, and K. J. Kirkby. "Investigation of gold nanoparticle radiosensitization mechanisms using a free radical scavenger

and protons of different energies". In: *Physics in Medicine and Biology* 59 (2014), pp. 6431–6443.

[43] I. Martínez-Rovira and Y. Prezado. "Evaluation of the local dose enhancement in the combination of proton therapy and nanoparticles". In: *Medical Physics* 42 (2015), pp. 6703–6710.

[44] R. Ahmad, G. Royle, A. Lourenço, M. Schwarz, F. Fracchiolla, and K. Ricketts. "Investigation into the effects of high-Z nano materials in proton therapy". In: *Physics in Medicine and Biology* 61.12 (2016), pp. 4537–4550.

[45] Chi-Jen Liu, Chang-Hai Wang, Shin-Tai Chen, Hsiang-Hsin Chen, Wei-Hua Leng, Chia-Chi Chien, Cheng-Liang Wang, Ivan M. Kempson, Y. Hwu, Tsung-Ching Lai, Michael Hsiao, Chung-Shi Yang, Yu-Jen Chen, and G. Margaritondo. "Enhancement of cell radiation sensitivity by pegylated gold nanoparticles". In: *Physics in Medicine and Biology* 55.4 (2010), pp. 931–945.

[46] Esra K. Kirakli, Gökhan Takan, Sinan Hoca, F. Z. B. Müftüler, Ayfer Y. Kılçar, and Serra A. Kamer. "Superparamagnetic iron oxide nanoparticle (SPION) mediated in vitro radiosensitization at megavoltage radiation energies". In: *Radioanalytical and Nuclear Chemistry* 315.3 (2018), pp. 595–602.

[47] Clara Emer, Laura S. Hildebrand, Bernhard Friedrich, Rainer Tietze, Rainer Fietkau, and Luitpold V. Distel. "In vitro analysis of superparamagnetic iron oxide nanoparticles coated with APTES as possible radiosensitizers for HNSCC cells". In: *Nanomaterials (Basel, Switzerland)* 13.2 (2023), p. 330.

[48] Nima Hamzian, Maryam Hashemi, Mahdi Ghorbani, Seyed Amir Aledavood, Mohammad Ramezani, and Mohammad Hossein Bahreyni Toosi. "In-vitro study of multifunctional plga-spion nanoparticles loaded with gemcitabine as radiosensitizer used in radiotherapy". In: *Iranian Journal of Pharmaceutical Research* 18 (2019), pp. 1694–1703.

[49] Stefanie Klein, Anja Sommer, Luitpold V. R. Distel, Winfried Neuhuber, and Carola Kryschi. "Superparamagnetic iron oxide nanoparticles as radiosensitizer via enhanced reactive oxygen species formation". In: *Biochemical and Biophysical Research Communications* 425.2 (2012), pp. 393–397.

[50] Yan Liu, Pengcheng Zhang, Feifei Li, Xiaodong Jin, Jin Li, Weiqiang Chen, and Qiang Li. "Metal-based nanoEnhancers for future radiotherapy: Radiosensitizing and synergistic effects on tumor cells". In: *Theranostics* 8 (2018), pp. 1824–1849.

[51] Anait S. Levenson and V. C. Jordan. "MCF-7: The first hormone-responsive breast cancer cell line". In: *Cancer Research (Chicago, Ill.)* 57.15 (1997), pp. 3071–3078.

[52] *MCF7 HTB-22 ™*. online; accessed 3 March 2020. URL: www.atcc.org.

[53] *Counting cells using a hemocytometer*. online; accessed 3 March. 2022. URL: https://www.abcam.com/protocols/counting-cells-using-a-haemocytometer.

[54] Pooja M. Tiwari, Komal Vig, Vida A. Dennis, and Shree R. Singh. "Functionalized gold nanoparticles and their biomedical applications". In: *Nanomaterials* 1 (2011), pp. 31–63.

[55] Sigma-Aldrich. *GNP Product specification*. online; accessed 4 April 2023. URL: https://www.sigmaaldrich.com/specification-sheets/218/123/765325-BULK_____ALDRICH__.pdf.

[56] Sigma-Aldrich. *Iron oxideProduct sheet*. online; accessed 4 April 2023. URL: https://www.sigmaaldrich.com/US/en/product/aldrich/747408.

[57] Jade D. Trono, Kazue Mizuno, Noritaka Yusa, Takehisa Matsukawa, Kazuhito Yokoyama, and Mitsuru Uesaka. "Size, concentration and incubation time dependence of gold nanoparticle uptake into pancreas cancer cells and its future application to X-Ray Drug Delivery System". In: *Journal of Radiation Research* 52.1 (2011), pp. 103–109.

[58] National Electrostatics Corporation (NEC). "AcceleratorManual". In: (2010).

[59] R Middleton. "A versatile high intensity negative ion source". In: *Nuclear Instruments and Methods in Physics Research* 220 (1984), pp. 105–106.

[60] Eric Maertz. *Fast Carbon-Ion and Proton Induced Electron Emission from Condensed-Phase Biological Targets*. Dissertation. East Carolina University, 2018.

[61] M.D. Ziegler J.F. Ziegler J.P. Biersack. *SRIM the stopping and range of ions in matter*. 2007. URL: www.SRIM.org.

[62] Namrita Lall, Cynthia J. Henley-Smith, Marco N. De Canha, Carel B. Oosthuizen, and Danielle Berrington. "Viability reagent, prestoBlue, in comparison with Other available reagents, utilized in cytotoxicity and antimicrobial assays". In: *International Journal of Microbiology* 2013 (2013), p. 420601.

[63] Thermo Fisher Scientific. *PrestoBlue ™ cell viability reagent*. URL: www.thermofisher.com/us/en/home/global/.

[64] *Processing absorbance data obtained using prestoblue viability reagent*. 2011. URL: www.lifetechnologies.com/prestoblue.

[65] R Core Team. *A language and environment for statistical computing*. ISBN 3-900051-07-0. R Foundation for Statistical Computing. Vienna, Austria, 2013. URL: `http://www.R-project.org/`.

[66] Christopher Michael Boyd. *Modification of cell survival rates by cerium oxide nanoparticles for exposure to proton radiation*. Dissertation. East Carolina University, 2017.

[67] Nathan B Carlson. *Protection and sensitization of human cells to proton radiation by cerium oxide nanoparticles*. Dissertation. East Carolina University, 2017.

A Appendix

A.1 Accelerator Repair

In July of 2021 the accelerator was brought up to atmosphere for an 8 month fix. Prior to bringing the accelerator tank up to air, the vacuum on the HE side of the accelerator beam line tube was at risk of coming above 1×10^{-5} torr. If this pressure was reached, the accelerator preforms an automatic shut down, suspending further use of the accelerator. The pressure in the HE side, should remain around 1 $\times10^{-7}$ torr while idle and around 1×10^{-6} torr while in use. In July of 2021 it was reported to be around 5.7×10^{-6} torr which was problematic.

When generating beam, the pressure in the HE side naturally rises based on the introduction of the N2 stripper gas. This potential rise in pressure would likely result in the automatic shutdown feature being activated.This necessitated a shutdown on July 8th 2021, and an 8 month troubleshooting process to identify and correct the cause of the elevated pressure issue. The elevated pressure on the HE side indicated there was a leak happening in the accelerator beam line tube within the tank of the accelerator pictured in Figure 1.1. The center accelerator beam tube is comprised of metal and ceramic ultra high vacuum connections. The suspicion was that one of these connections had worn with time and started a small slow leak. That gave the indication of where to start testing for the leak. [58].

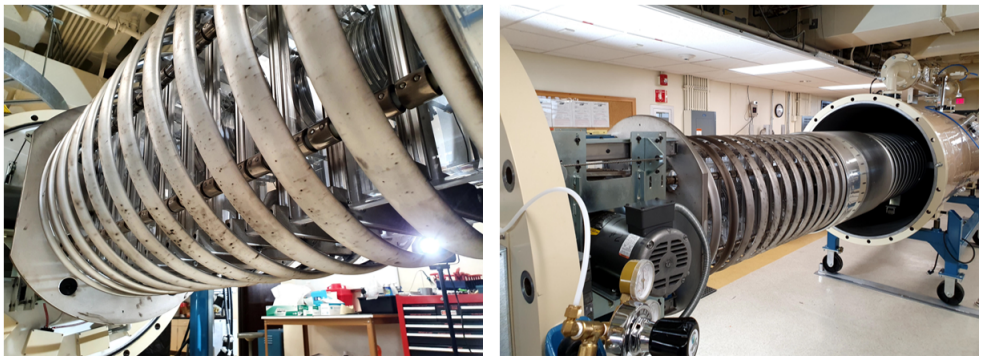

Figure 1.1: Shows the state of the accelerator when brought up to air. In each panel there is evidence of a black substance on the surfaces, which was caused by a failure in the terminal chain pulley bearing.

In order to start the diagnostic process, one of the first things that needed to happen was to roll the accelerator beam tube out of the tank, which is pictured in figure 1.1. To start this process, several steps needed to be executed. Initially, the lab needed to be organized and a special space needed to be designated for all of the materials that were to be taken apart. This was done to prevent loss or confusion of where the part came from. Once a space was cleared the insulating gas, Sulfur Hexafloride (SF_6) gas needed to be pumped out of the tank and stored in appropriate containers in the lab. Post storing the FS_6 the accelerator beam tube needed to remain under vacuum. It is blocked on the low energy bellows with a conflat fixture that is sealed with a copper gasket to prevent any leakage. Once the low energy side was capped off, the high energy bellows were also sealed off in a similar fashion.

This allowed the accelerator tank to be rolled out from the rest of the beam line tubes. It is important to note that in order to cap off the section of the accelerator beam tube that needs to be checked, the turbo and rough pump systems attached on the LE and HE side of the accelerator needed to be powered down and let up to air to remove the tank. If this is not done the conflat connectors will not come apart and the accelerator tank will not be able to be rolled out. Once the HE and LE sides of the tank were sealed off the removable tracks to move the tank were placed down. This allowed the tank to be slowly pushed out away from the beam line on either side of the bellows attachments. Once the tank is rolled out the 1 1/2" bolts that sealed the tank together on the HE side were removed and the accelerator beam tube was separated from the tank as pictured in figure 1.2, and the trouble shooting began.

Figure 1.2: Shows the panel of the accelerator tank on the HE side that had to be removed to separate the tank from the beam line tube.

As discussed the only indication of a problem was elevated HE pressure. This indicated a leak was occurring in the accelerator beam tube, but the location was unclear. The HE side of the accelerator covers roughly 1.5 m of beam line made up of ceramic and metal connections. Over time the metal and ceramic connections can start to leak, which will increase the beam line pressure. The best way to determine a leak in a vacuum system is to introduce a gas or alcohol into the vicinity of the leak and monitor the pressure read out for a spike. When alcohol or a gas like helium (He) is introduced into a vacuum system, it creates a subtle spike in the overall pressure when leaked into the system. When the leak is not identifiable with alcohol the next best thing is to use a Helium leak detector. The He leak detector (pictured in Figure 1.3) is a device that will connect to a section of beam line that is meant to be held under vacuum. It is fit with a rough and turbo pump through KF flanges, and can be connected to the section of beam line that may have a leak. The pump system helps maintain and monitor the pressure in the section in question. A He

tank is also required to pin point the leak. The left panel of Figure 1.3 shows the interface of the detector while the right shows a zoomed out view with the rough pump connected. When running the detector it can be set to a vacuum threshold via the knob on the front panel. When the pressure is exceeded because the He infiltrated the vacuum system, it will sound an alarm, indicating the location of the leak. It is important to note that this is a slow process, and needs just a small amount of He, because of that the He tank is fitted with a fine needle nose nozzle with a valve on it to slowly filter small spurts of He from the tank. The needle nose fitting helped to prevent He exposure to large portions of the HE side, which would make identifying the leak locations difficult. The needle nose fitting allowed small amounts of He to be released at each individual metal-ceramic connection and then the system was monitored for subsequent spikes in pressure. This systematic method was meticulously applied throughout the HE section until the leak was located and subsequently sealed.

Figure 1.3: The helium detector, this device is fitted with both a rough pump and turbo pump to pull low vacuum for any device it is connected to. The left panel shows the control interface for the detector, and the right panel gives a full view of the detector.

In order to seal the leak a special paint/glue like substance called Glyptal[4] was purchased. Glyptal is a red paint-like substance used primarily to seal the internal surfaces of an engine block. Next the task was to insert the sealant all around the connection to assure the leak would not occur again. To apply this material a clean oil free surface was needed. This meant a thorough cleaning of the outer layer of the beam line and surrounding surfaces of the accelerator needed to happen. This was done with special clothes that do not leave behind any residue. Once the surfaces of the beam line tube were cleaned the lab engineer utilized a pressurized needle nose syringe loaded with Glyptal. The syringe, shown in figure 1.4, steadily pumped out the Glyptal into the metal to ceramic connection to reinforce the

[4]The web site for purchasing and information about the product; http://www.glyptal.com/

leak, recreating a vacuum tight seal. This was left to dry and the next day the He detector was used again to confirm the seal was holding.

Once the leak was assessed and sealed the process of reconstruction could begin. This started with a final cleaning/wipe down of the accelerator tank, and the exoskeleton pictured in Figure 1.1. The pellet chains also needed to be removed and cleaned of any existing soot. Once cleaned the pellet chains are placed back onto the accelerator, where they are run from the high voltage terminal to the ground end of the accelerator (Figure 1.1 top panel on the left). Once the chains were re-strung they needed to be run/assessed to ensure appropriate tightening and oriented such that no collisions within would occur during rotation. Upon successful rotation, the accelerator was ready for one final cleaning, the accelerator was re-assembled and brought down to vacuum.

Once the appropriate vacuum was achieved, the conditioning process was started. The accelerator is powered, and beam is generated with the Cs^+ and the operating voltage is slowly brought up to 2 MV, the highest operating voltage. This process is known as conditioning the accelerator. Conditioning was a slow process because as the accelerator was up to atmospheric pressure, particulates and gas were absorbed to the surfaces and when a voltage is applied the materials can become ionized. This can cause micro-discharges to occur in vacuum which in turn limits the voltage [58]. Thus, the voltage had to be increased slowly to allow the particulates and and gas to burn off. This process was repeated slowly for a couple of weeks until the maximum operational voltage was reached, implying the accelerator was ready for experimental use again.

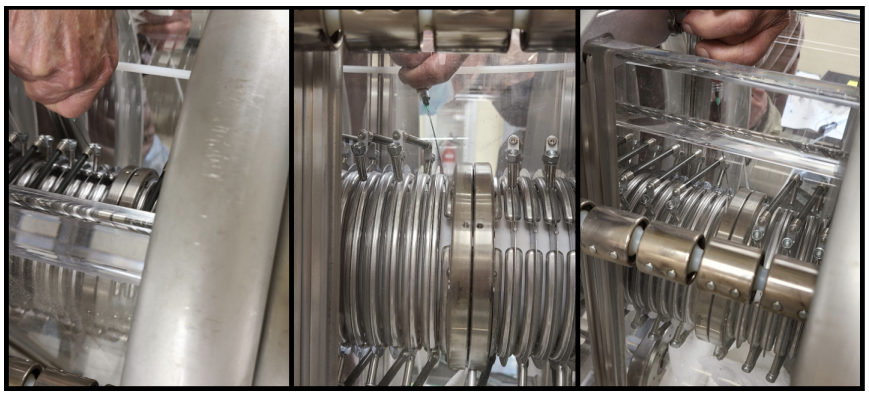

Figure 1.4: Each panel depicts the introduction/placement of the Glyptal paint which was used to seal the leak on the HE line.